Aspect-ratio-dependent phase transitions and concentration fluctuations in aqueous colloidal dispersions of charged platelike particles

Daisuke Yamaguchi,[1] Nobuyoshi Miyamoto,[2] Takako Fujita,[3] Teruyuki Nakato,[3,*] Satoshi Koizumi,[1,†] Noboru Ohta,[4] Naoto Yagi,[4] and Takeji Hashimoto[1,‡]

[1]*Quantum Beam Science Directorate, Japan Atomic Energy Agency, Tokai, Naka, Ibaraki 319-1195, Japan*

[2]*Department of Life, Environment and Materials Science, Fukuoka Institute of Technology, 3-30-1 Wajiro-higashi Higashi-ku, Fukuoka 811-0295, Japan*

[3]*Division of Bio-Applications and Systems Engineering (BASE), Institute of Symbiotic Science and Technology, Tokyo University of Agriculture and Technology, 2-24-16 Naka-cho, Koganei-shi, Tokyo 184-8588, Japan*

[4]*Japan Synchrotron Radiation Research Institute, SPring-8 Kouto, Sayo, Hyogo 679-5198, Japan*

(Received 19 January 2011; revised manuscript received 14 September 2011; published 18 January 2012)

Phase transitions of aqueous colloidal dispersions of charged platelike particles of niobate nanosheets were investigated as a function of the aspect ratio (r_{asp}) and particle volume concentration (ϕ_p) by means of small-angle neutron scattering and small-angle x-ray scattering. The results elucidated the following three pieces of evidence: (1) the macroscopic phase separation of the dispersions into an isotropic phase and a liquid crystalline (LC) phase under the conditions of (a) varying r_{asp} ($1.3\times10^{-4} \leqslant r_{asp} \leqslant 2.5\times10^{-3}$) at a constant $\phi_p = 0.01$ and (b) varying ϕ_p ($0.01 \leqslant \phi_p \leqslant 0.025$) at a constant $r_{asp} = 2.5\times10^{-3}$, a mechanism of which is proposed in the text, where $r_{asp} \equiv d/\overline{L}$, with d and $\overline{L}$ being thickness and the average lateral size of the plates, respectively; (2) the r_{asp}-induced phase transition of the LC phase from a nematic phase to a highly periodic layered phase, the line shapes of the scattering peaks of which were examined by Caillé's analysis, upon increasing r_{asp} under the condition (a); (3) the LC phase having remarkable concentration fluctuations of the particles which are totally unexpected for the conventional lyotropic molecular LC but which are anticipated to be general for the platelike colloidal particles.

DOI: 10.1103/PhysRevE.85.011403 PACS number(s): 82.70.Dd, 61.30.−v, 64.75.Xc

I. INTRODUCTION

This work was motivated by our previous work [1], which elucidated the intriguing a mass-fractal-like concentration fluctuations existing in the (macroscopically uniform) lyotropic liquid crystalline phase (LC) composed of aqueous dispersions of exfoliated niobate nanosheets. The nanosheets, as one of the charged platelike colloidal dispersions, had a particle size characterized by $d = 1.6$ nm and $\overline{L} = 3.2$ μm and at a particular particle volume concentration $\phi_p = 0.032$, where d and $\overline{L}$ are the thickness and the average lateral size (L) of the sheets, respectively. We aim to clarify universality of the concentration fluctuations in the LC of the nanosheet dispersions, which are totally unexpected whatsoever for the conventional lyotropic molecular LC, by extending our observations on the same nanosheets to a wider range of the parameter space of aspect ratio ($r_{asp} \equiv d/\overline{L}$) and ϕ_p: (a) $1.3\times10^{-4} \leqslant r_{asp} \leqslant 2.5\times10^{-3}$ at a constant $\phi_p = 0.01$ and (b) $0.01 \leqslant \phi_p \leqslant 0.037$ at a constant $r_{asp} = 2.5\times10^{-3}$. We report also the detail of the phase transitions found in the systems: macroscopic phase separation into isotropic and LC phases and the r_{asp}-induced phase transition within the LC phase.

Formation of LC phases in aqueous dispersion of charged colloidal particles having large shape anisotropies has been an attractive issue over a century, since subtle changes in physical and chemical properties of the constituent particles as well as those in effective interactions of those particles with water have a great influence on the thermodynamic stability of the phases, such as nematic, smectic or lamellar, cholesteric, etc. [2,3]. Onsager's seminal work on rodlike particles [4] successfully predicted the nematic order by applying the method of the virial expansion to the system having only the hard-core potential between the particles. Since then various theoretical and computational studies have contributed to formation of the LC phases consisting of rodlike particles [5].

In comparison with the rodlike particles, much less theoretical and simulation studies have been conducted on the LC phase behavior of platelike particles [6–9]. Nevertheless, a systematic phase diagram of platelike particles, which includes isotropic, nematic, columnar, cubic, and solid phases [10], was constructed by Veerman and Frenkel [11]. Furthermore, Bates and Frenkel [12,13] incorporated the influences of polydispersity of size and shape of the plate into the nematic-isotropic phase transition. Turning our attention to the experimental studies, numbers of studies have been devoted to the LC phase behavior of platelike particles [14–26]. In particular, in a recent decade there have been important findings on the formation of columnar [18–20,23,25] and lamellar [21,24,26] or smectic [27] phases.

In this work, our aim is to explore isotropic, nematic, and some kinds of layered phases (denoted as Lay hereafter) related with the lamellar phase [28], formed in the aqueous dispersions of the particular niobate nanosheets which have an extremely larger shape anisotropy than the conventional disk- or sheet-like molecular systems. For the sake of clarity,

*Present address: Department of Material Science, Graduate School of Engineering, Kyushu Institute of Technology, Sensui-cho, Tobata-ku, Kitakyushu-shi, Fukuoka 804-8550, Japan.

†Present address: Faculty of Engineering, Ibaraki University, Nakanarusawa-cho 4-12-1, Hitachi-shi, Ibaraki 316-8511, Japan.

‡Professor emeritus, Kyoto University, Kyoto 606-8501, Japan & Honorary Chair Professor, National Tsing Hua University, Hsinchu 30013, Taiwan.

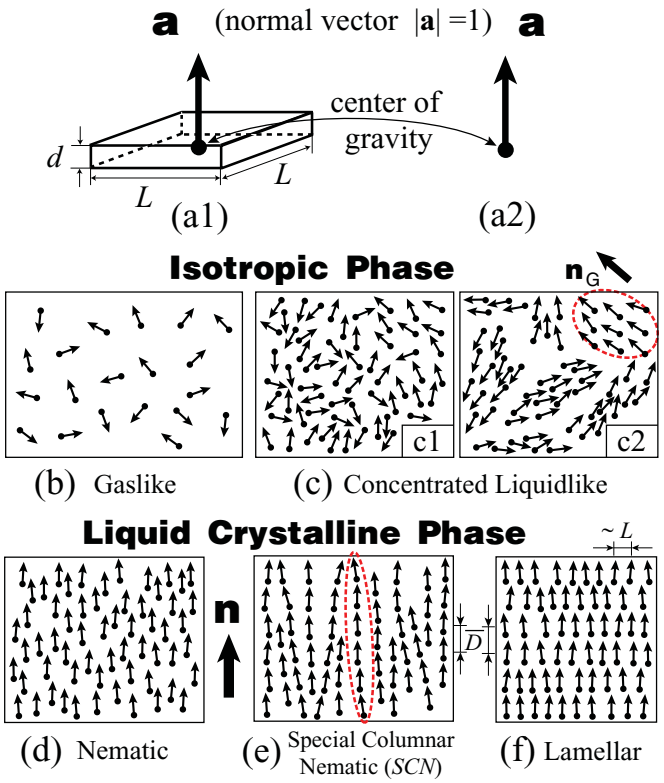

FIG. 1. (Color) Schematic illustrations of the phases investigated in this study. (a) A platelike particle (a1) and its coarse-grained structural entity (a2). The isotropic phase of platelike particles is further classified into a dilute "gaslike state" (b) and a concentrated "liquidlike state" (c). Two possible states may be considered for (c): (c1) macroscopically random orientation of **a** with no orientation correlation and (c2) the orientation correlated within small grains but the grains themselves randomly oriented in space, giving rise to a macroscopically random orientation of **a**. The LC phase with a macroscopic orientation of **a** is classified into nematic (d), *special* columnar nematic (SCN) (e), and lamellar (f) phases. Note that the length L and $\overline{D}$ (the average spacing between the platelike particles along **a**) are shortened and enlarged, respectively, for the sake of convenience in the illustrations (c1), (c2), and (d) to (f).

the definition of each phase to be expected for such sheets is schematically presented in Fig. 1. First, the platelike particle is defined by its "normal vector" **a**, which is a unit vector locating at the center of gravity of the particle and having the direction normal to the plate surface, and sizes d and L parallel and perpendicular to **a**, respectively, as shown in part (a1) in Fig. 1. The platelike particle can be coarse grained by an arrow shown in part (a2) with its orientation and center of gravity specified by the vector **a** and by the one end of the arrow, respectively. Then, the following isotropic and LC phases are considered for assemblies of the plates, as depicted in Figs. 1(b)–1(f), respectively. To simply capture the characteristics of each phase, all the platelike particles are supposed to exist in two-dimensional space with their **a**'s being confined in the plane of the paper.

Provided that the isotropic phase is simply defined as a state where the vector **a** is randomly oriented, the following two states may be considered, depending on the positional and orientation correlation of **a**, as shown in Figs. 1(b) and 1(c): (i) When the particles are dilute enough to be isolated each other, they are in a gaslike state having no positional and orientation correlations [Fig. 1(b)], while (ii) when the concentration of the particles becomes large, the particles have a liquidlike state having a short-range positional and orientation correlations [Fig. 1(c)]. The crossover from a gaslike state to a liquidlike state should occur around the overlapping concentration, $\phi_p{}^*$, where the platelike particles start to overlap each other and are forbidden to make a free rotation due to the excluded volume effect. Given a completely rigid platelike particle, $\phi_p{}^*$ is simply estimated by the following equation, $\phi_p^* = (3/\pi\sqrt{2})d/L$ in the case of $r_{asp} \ll 1$. Generally bendings of the particles occur at a length scale larger than the persistent length l_p. In this case, $\phi_p{}^*$ can be expressed as $\phi_p^* = (3/\pi\sqrt{2})d/l_p$ by replacing L with l_p.

The nematic and lamellar phases, depicted in Figs. 1(d) and 1(f), respectively, are the LC phases which we aim to intensively investigate in this study. When the spatial distribution of **a**'s are considered as the coarse-grained units of the platelike particles, we can easily recognize the fact that the LC phase of the platelike particles have characteristics identical to the LC phase of the rodlike particles or molecules. In the nematic phase (d), **a**'s have the orientation order with respect to the director **n**, which specifies the direction of an average orientation of **a**'s, but no positional order. In the lamellar phase (f), **a**'s are arranged in layers so that in addition to the orientation order, there exists a long-range positional order too between the layers (average periodicity, $\overline{D}$), though there is only a short-range liquidlike positional order along the layers in the direction perpendicular to **a**'s.

There is another possible state possessing a long-range positional order of **a**'s along their axes **a**'s comparable to lamellar phase but no coplanar structure along the direction perpendicular to **a**'s as in the case of lamellar phase. This state (e) corresponds to a special case of the so-called "columnar nematic phase" [29–31] and is hereafter denoted as the "special columnar nematic (SCN) phase." The word "special" is used to emphasize a special feature in the columnar nematic, which arises from the long-range positional order along the columnar axis. Therefore, SCN should be distinguished from both the lamellar phase and the nematic phase.

In order to further clearly define the three states (d), (e), and (f) in Fig. 1, the average interparticle distances in the directions perpendicular to **a** ($\overline{D_x}$ and $\overline{D_y}$) and in the direction parallel to **a** ($\overline{D_z}$, i.e., $\overline{D_z} \equiv \overline{D}$ throughout this paper) are introduced, as shown in Figs. 2(a) and 2(b). Figure 2(a) also shows the average displacement tensor $\Delta\widetilde{D} = (\Delta D_{ij})$ $(i, j = x, y, z)$, which characterizes the standard deviations of the centers of mass of the nearest-neighbor particle with respect to a given particle at the origin O from the average spacing $\overline{D_i}$ $(i = x, y, z)$ along jth direction $(j = x, y, z)$. Then the degree of positional order for the centers of mass of the sheets is characterized by g_D tensor defined by, $\widetilde{g}_D \equiv (g_{ij}) \equiv (\Delta D_{ij}/\overline{D_i})$.

Upon using g_{ij}, the definitions of the nematic, lamellar and SCN phases become rather simple and more quantitative as follows: For the nematic phase having no positional order, all of g_{ij} components is sufficiently large so that no diffraction maximum can be observed, satisfying the criterion of $g_{ij} \geqslant 0.35$ found by Hosemann and Bagchi [32]. Note that the criterion of $kg_{zz} \leqslant 0.35$ corresponds to the one where the

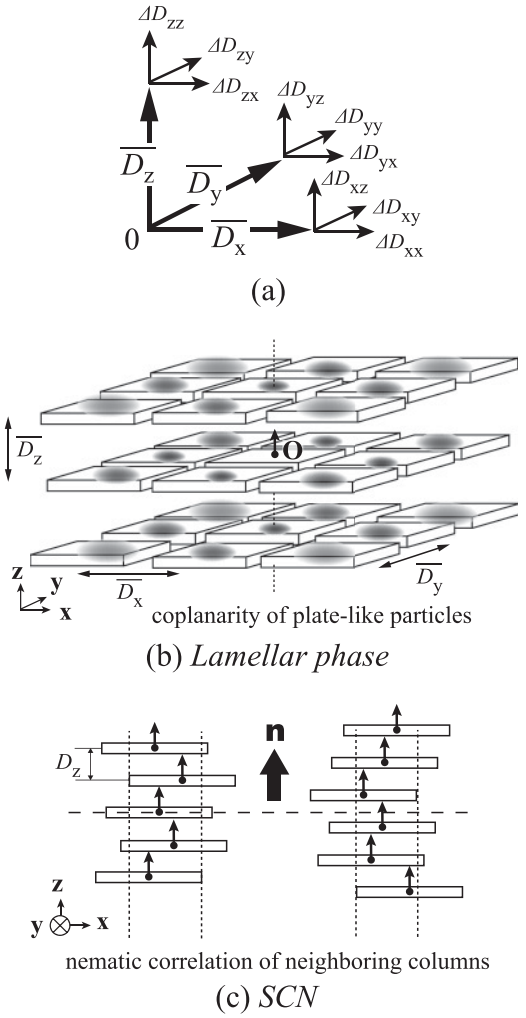

FIG. 2. Schematic illustrations of the lamellar phase (b) and the SCN phase (c). (a) Displacement tensor $\Delta\widetilde{D} = (\Delta D_{ij})$ $(i,j = x, y, z)$ for the nearest neighbour intersheet distance along the x, y, and z directions from the average intersheet distances $\overline{D_x}$, $\overline{D_y}$, and $\overline{D_z}$. The lamellar phase (b) is characterized by a "coplanarity" of centers of mass of the sheets in the x-y plane. The gray zone qualitatively displays the probability distribution $P(x, y, z)$ for centers of mass of the sheets with respect to the given sheet at an origin O. The coplanarity demands the spread of P along the z direction being much smaller than that along the x and y direction. A possible order for the SCN phase (c) is characterized by no positional correlation of the sheets between neighboring columns, within which the sheets are stacked with a high periodicity, that is, with a small ΔD_{zz}.

kth-order diffraction peak appears along the z direction and that the criterion of $kg_{zz} \geqslant 0.35$ corresponds to the one where the kth-order peak disappears. However, the lamellar phase [Fig. 2(b)], which must have a coplanarity of the platelike particles in the x-y plane, induces a constraint of a small $g_{iz} \equiv \Delta D_{iz}/\overline{D_i}$ $(g_{iz} < 0.35)$ $(i = x, y, z)$, but a relatively large $g_{xj} \equiv \Delta D_{xj}/\overline{D_x}$ $(g_{xj} \geqslant 0.35)$, $g_{yj} \equiv \Delta D_{yj}/\overline{D_y}$ $(g_{yj} \geqslant 0.35)$, and $g_{zj} \equiv \Delta D_{zj}/\overline{D_z}$ $(g_{zj} \geqslant 0.35)$ $(j = x, y)$. For the case of the SCN phase [Fig. 2(c)], all g_{ij} $(i, j = x, y, z)$ components, except for $g_{zz} \equiv \Delta D_{zz}/\overline{D_z}$ (<0.35), have a large value $(g_{ij} \geqslant 0.35)$, due to the nematic correlations of the centers of mass of plates in the neighboring columns. However, the centers of mass of the platelike particles must be confined in the columns, giving rise to $(\Delta D_{zx}$ and $\Delta D_{zy}) \leqslant R_{\text{col.}}$ (radius of the column), and g_{zz} is small due to the special feature of SCN.

From the practical viewpoint, the scattering methods easily distinguish the difference in the long-range positional order or correlations of the particles along the direction parallel to **n**; almost no periodicity in the nematic phase (d), but a clear periodicity in the SCN phase (e) and in the lamellar phase (f). However, the difference between the lamellar phase (f) and the SCN phase (e) is hardly distinguished by the scattering methods employed in this study, simply because the length scale covered is not sufficiently large so as to characterize existence of the coplanarity of the sheets. Hence, in this paper, we do not distinguish the lamellar and SCN phases and generally refer to both of the lamellar and SCN phases as "layered phase" or "Lay" for the sake of brevity. We would like to stress here that Lay has a common feature of the lamellar and SCN phases in forming a periodic structure of sheets along **a**, but that Lay is distinctly different from the nematic and isotropic phases.

As for the concentrated liquidlike state shown in Fig. 1(c), we may be able to visualize two possible states (c1) and (c2) which have the same short-range liquidlike positional correlation but different orientation correlations. Note that (c1) and (c2) have schematically the same spatial distribution of the centers of gravity of the particles. The state (c1) essentially has a random "orientation correlation (OC)", while the state (c2) has a nonrandom OC. The nonrandom OC means that the correlations of the two **a**'s at a displacement vector **r** apart depends not only on **r** but also on the polar angle between **r** and one of **a** from which the OC is to be considered, while the random OC means that the OC is independent of the polar angle [33]. The state (c2) comprises small grains within which **a**'s have OC, but **a**'s belonging to different grains do not have the OCs. The positional and OCs within the small grains are essentially equal to those shown in part (d) for the oriented nematic phase. The small grains are characterized by the director $\mathbf{n}_{\text{G}}$ but $\mathbf{n}_{\text{G}}$ is randomly oriented macroscopically in part (c2).

Although the state (c2) is classified as the isotropic phase in Fig. 1, the state may be characterized by a nematic phase composed of randomly oriented grains also, which are created through a spatial distribution of defects of the so-called disclination lines. **a**'s in the grain can have an orientational order parameter with respect to $\mathbf{n}_{\text{G}}$, which is close to the orientational order parameter in part (d). Upon increasing the density of the disclination lines, the grain becomes small, the free energy of the system increases, and the state (c2) eventually approaches to the state (c1) in the limiting case. If the grains are sufficiently large, the state (c2) can be reasonably assigned to the nematic phase with a macroscopically random orientation of $\mathbf{n}_{\text{G}}$'s. However, it is a problem at the present stage that the critical size of the grains, above which the state (c2) can be regarded as the nematic phase with the random orientation of $\mathbf{n}_{\text{G}}$'s, is not well defined.

To make a systematic discussion for the phase behavior of the platelike particles in the parameter space of ϕ_{p} and L, it is convenient to introduce r_{asp}. The main achievement of a systematic simulation study [11] can be briefly summarized as follows; a sequential transition involving isotropic-nematic, nematic-columnar, and columnar-solid transitions takes place with increasing ϕ_{p} for $r_{\text{asp}} \leqslant 0.14$, whereas a simple

isotropic-solid transition with missing the nematic and columnar phases appears for $r_{asp} \geqslant 0.24$. The experimental verification of the computational prediction seems quite crucial. However, up to now a clear piece of experimental evidence for the phase transition in the LC phase induced by changing r_{asp} has not been reported yet, probably because of a variety of practical difficulties in the experiments.

For instance, the clear-cut pieces of evidence for isotropic-nematic [20,34–39], isotropic-lamellar [21,40], and a sequential transition involving isotropic-nematic and nematic-lamellar transitions [26] with increasing ϕ_p at a particular r_{asp} (in the range satisfying $1.1 \times 10^{-3} \leqslant r_{asp} \leqslant 7.1 \times 10^{-2}$) have already been obtained by using the scattering method. However, due to the difficulty in preparing a wide variety of size-controlled particles, the experimental studies attempting to elucidate systematically the r_{asp} dependence of the phase behavior are rather minor [22,23,34–38]. Among these, Ref. [23] employed the particles with a fixed size but the controlled "effective" r_{asp} ($r_{asp,eff}$), indirectly through the variation of Debye screening length κ^{-1}. Upon increasing κ^{-1}, $r_{asp,eff} \sim (d + \kappa^{-1})/(L + \kappa^{-1})$ also is increased. As κ^{-1} is in inversely proportional to the ionic strength (n), the increasing of $r_{asp,eff}$ was attained by decreasing n. Based on this method van der Beek *et al.* [23] succeeded in finding the fact that the transition involved by increasing ϕ_p depends on $r_{asp,eff}$: isotropic-nematic for $r_{asp,eff} \leqslant 0.14$ and isotropic-columnar for $r_{asp,eff} \geqslant 0.14$.

On the other hand, Michot and co-workers [34–38] systematically investigated the phase transitions occurred on the various platelike clay particles induced by increasing ϕ_p for a given range of r_{asp} and n. Michot *et al.* [34] and [35] employed nontronite clay particles in the range of r_{asp} satisfying $1.5 \times 10^{-3} \leqslant r_{asp} \leqslant 4.5 \times 10^{-3}$ and found only isotropic-nematic transition with increasing ϕ_p. Note here that the r_{asp} is taken as the ratio of the (average) thickness to the (average) length of the longer lateral edge, since the nontronite clay particles possess a lath shape. Succeedingly, Paineau *et al.* [36] aimed at the phase transitions occurred on a disk-shaped beidellite clay particle in a relatively narrow range of $3.0 \times 10^{-3} \leqslant r_{asp} \leqslant 3.4 \times 10^{-3}$ and clarified the nature of fist-order isotropic-LC transition. It is worth mentioning that the LC phase had a strikingly high periodicity close to the Lay phase discussed in this work, although the authors regard and describe the observed LC phase as a nematic phase.

Very recently, Paineau *et al.* summarized a general feature of isotropic-LC as well as sol-gel transitions observed on various platelike clay particle systems in the parameter space of r_{asp} and n, where n is in mol/L within the limits of $2.4 \times 10^{-3} \leqslant r_{asp} \leqslant 1.6 \times 10^{-2}$ and $10^{-5} \leqslant n \leqslant 10^{-3}$ [37,38]. Michot and co-workers intensively investigated the positional order among the platelike particles in the LC phase as a function of r_{asp}, n [34–37] and the type of clay as well [37]. As a consequence, they claimed that the positional order was disrupted with decreasing r_{asp} (or increasing average particle size) [35,37]. However, the classification of the LC phase into the nematic phase and the Lay phase was out of their aim in the whole series of their study [34–38].

Miyamoto and Nakato [22] elucidated a lot of features on the phase behavior with ϕ_p for the same material used in this study at a wide range of r_{asp}, $2.3 \times 10^{-4} \leqslant r_{asp} \leqslant 1.2 \times 10^{-2}$. However, the identification of the types of LC phase was impossible, owing to the naked-eye observation.

This study demonstrates a clear piece of experimental evidence concerning a sharp transition from the nematic to Lay phase being simply brought about by increasing r_{asp} or reducing $\overline{L}$ at a constant d and at a constant ϕ_p [41]. For the observation of this transition the small-angle scattering technique played a crucial role. Our experimental results are summarized as follows: At a constant $\phi_p = 0.01$, the dispersion underwent a transition from a isotropic/nematic coexisting state to a isotropic/Lay coexisting state with increasing r_{asp} above the critical value of 2×10^{-3} ($\overline{L} = 0.8\ \mu$m). Note that $\phi_p = 0.01$ satisfies the condition of $\phi_p \geqslant \phi_p{}^*$ for all the examined r_{asp} in this study, ranging $1.3 \times 10^{-4} \leqslant r_{asp} \leqslant 2.5 \times 10^{-3}$ [42]. We carefully investigate also the universality of the concentration fluctuations of the platelike particles in the LC phase.

II. EXPERIMENTAL METHODS

The platelike particles employed in this study were $[Nb_6O_{17}]^{4-}$ bilayer units exfoliated from $K_4Nb_6O_{17}$ layered single crystals [22,43,44]. The particles were quadrilateral discs with a constant thickness of $d = 1.6$ nm, whereas L varied from dozens of microns to submicrons. The particles possess extremely small r_{asp} and look like sheets rather than discs and hence we designate them as "nanosheets." The process for obtaining the nanosheets has been well established in the literature [22,43–45] and is composed of three steps: (i) a high-temperature solid-state synthesis of $K_4Nb_6O_{17}$ single crystals, (ii) the exchange of potassium cations (K^+) in the crystals partly by propylammonium ion ($C_3H_7NH_3{}^+$) in an aqueous solution of propylamine hydrochloride to bring about the exfoliation of $[Nb_6O_{17}]^{4-}$ unit composed of bilayers, and (iii) a thorough dialysis of the resultant nanosheets with pure water to remove excess counterions (i.e., K^+, $C_3H_7NH_3{}^+$).

We prepared three kinds of the nanosheet specimens having different $\overline{L}$ as shown in Fig. 3. Other parameters, such as pH ($\sim$10) and n (at the order of 10^{-4} mol/L) in the aqueous suspensions, were set in common. To change $\overline{L}$, we followed the method described in the previous report [22]: The original nanosheet particles having $\overline{L} = 12.2\ \mu$m [Fig. 3(a)] were chopped into smaller pieces by holding the suspension under ultrasonic vibration. $\overline{L}$ can be controlled by the duration of sonication, while the polydispersity of L (g_L) did not show distinct change, where g_L is defined as $g_L = \sigma_L/\overline{L}$ and σ_L denotes the standard deviation of L with respect to $\overline{L}$. Each specimen is hereafter denoted by its $\overline{L}$ value in μm, that is, 12.2, 0.98, and 0.65, and possesses its own g_L of 82%, 55%, and 53%, respectively [see Figs. 3(a)–3(c)].

The nanosheet suspensions were placed into quartz cells having an internal cross section of 1 mm (thickness) $\times$ 8 mm (width) and a height of 40 mm. The suspensions were aged in the cell, held upright as shown in Fig. 4(a), for a period of up to more than 1 year to attain the equilibrium state as much as possible, and observed between the crossed polarizers after the aging periods of 1 month and 1 year. To investigate the mesoscopic scale structure of those nanosheet suspensions, we employed a combined small-angle scattering method which

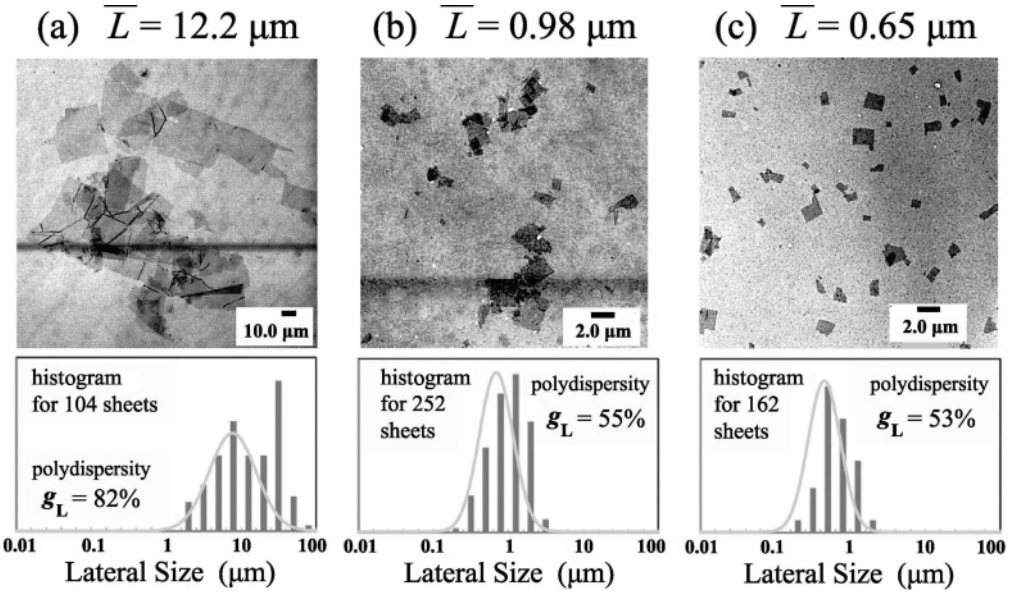

FIG. 3. Nanosheet specimens having different mean lateral size ($\overline{L}$): (a) 12.2 μm, (b) 0.98 μm, and (c) 0.65 μm. Typical TEM images and histograms of the lateral size are shown on the top and bottom panels, respectively. The gray curves in the bottom panels represent log-normal distribution function having the arithmetic mean of $\overline{L}$ and arithmetic standard deviation of σ_L.

utilizes in concert both small-angle neutron (SANS) and x-ray scattering (SAXS) methods. SANS measurements were performed on the SANS-J-II spectrometer at the research reactor JRR-3 (Tokai, Japan) [46] having the accessible q range from 0.03 to 1 nm^{-1}. Hereafter, q denotes magnitude of scattering vector defined by $q = [4\pi \sin(\theta/2)]/\lambda$, where θ and λ are the scattering angle and wavelength of incident beam, respectively. As the incident neutron beam was passed through a set of 8-mm pinholes in front of the specimen, we observed the averaged microstructure of the specimen within the irradiated area of ~50 mm^2 and the irradiated volume ~50 mm^2 × 1 mm.

SAXS measurements were performed at the beamline BL40XU at the SPring-8 synchrotron radiation facility (Hyogo, Japan) [47]. The sample cells employed for the SAXS measurements were both capillary tubes of 0.6 mm diameter and quartz cells of 1 mm (thickness) × 8 mm (width), as described above. With the quartz cells, the specimens having different $\overline{L}$'s were measured (cf. Fig. 4), while the capillary tubes were used to examine ϕ_p dependence of SANS and SAXS profiles (related to Fig. 6). The suspensions placed in the capillary tubes were aged also by holding the tubes upright for 3 weeks before the measurements. In contrast to SANS measurement, we could obtain a scattering signal from quite a narrow area of ~30 μm^2 of the specimen with the SAXS experiment, in which the incident x-ray beam was passed through a 5-μm pinhole [48], though the size of the irradiated volume along the propagation direction of the beam is not particularly small but a conventional value (0.6 or 1 mm). The accessible q range in the SAXS experiment is from 0.1 to 2 nm^{-1}.

III. RESULTS AND DISCUSSION

The phase behavior of the nanosheet suspensions was studied as a function of two parameters $\overline{L}$ and ϕ_p; (1) $\overline{L}$ (or r_{asp}) dependence was investigated at a constant ϕ_p of 0.01, and (2) ϕ_p dependence was examined on the specimens having the smallest $\overline{L}$ (= 0.65) or the largest $r_{asp} = 2.5\times10^{-3}$. The previous study [22] has already elucidated the general trend of phase behavior of the nanosheet suspensions: With increasing ϕ_p at given values of $\overline{L}$ ranging from 0.15 to 7.8 μm, the nanosheet suspensions transformed from the isotropic phase to the LC phase through the coexistence phase intervening between the isotropic phase and the LC phase, though the type of the LC phase was not identified at all. Thus, we should define two transition points ϕ_I and ϕ_{LC} with respect to ϕ_p, where ϕ_I denotes the critical concentration for the transition from the isotropic phase to the isotropic/LC coexisting phase, and ϕ_{LC} denotes that from the coexisting phase to the LC phase.

A. $\overline{L}$ (or r_{asp}) dependence at fixed $\phi_p = 0.01$

Some typical results on $\overline{L}$ dependence of the dispersions at a given $\phi_p = 0.01$ are shown for $\overline{L}$ = 12.2, 0.98, and 0.65 ($r_{asp} = 1.3\times10^{-4}$, 1.6×10^{-3}, and 2.5×10^{-3}) in Fig. 4, where panels (a), (b), and (c) present the macroscopic appearance of the dispersion under crossed polarizers, SAXS patterns, and the radial SAXS and SANS profiles, respectively. In Fig. 4(a) the dispersions shown in parts (α), (β), and (γ) are those with $\overline{L}$ = 12.2, 0.98, and 0.65 observed after 1 year aging, while those in parts (α'), (β'), and (γ') are the respective dispersions observed after one month aging. The dispersions (α), (β), and (γ) clearly show two phases with a macroscopic interface highlighted by the bright arrow: the upper dark (or transparent) phase and the lower bright phase, where the darkness or the brightness is expected to be due to strength of the depolarized light scattered intensity in each phase. The upper and lower phases were further designated as (i) and (ii) for $\overline{L}$ = 12.2 (α), (iii) and (iv) for $\overline{L}$ = 0.98 (β), and (v) and (iv) for $\overline{L}$ = 0.65 (γ), respectively. These indices (i)–(vi) are commonly used for parts (b) and (c) to specify the phases, from which the

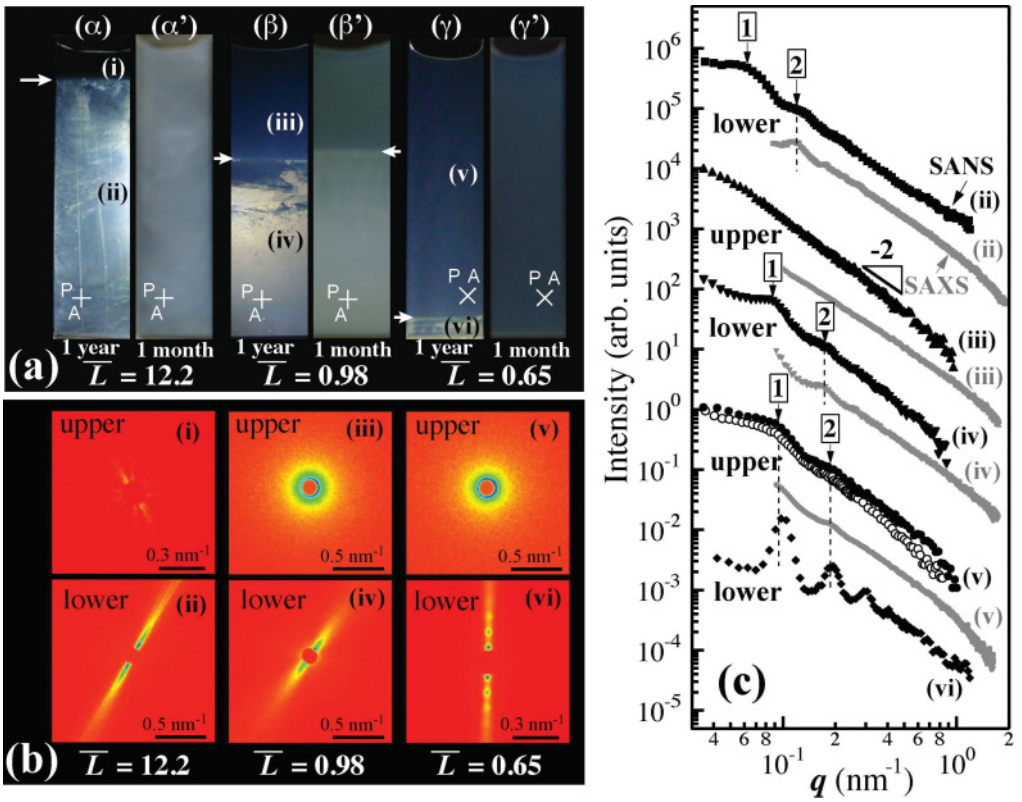

FIG. 4. (Color) The influence of $\overline{L}$ upon the near-equilibrium state of the nanosheet suspensions at $\phi_p = 0.01$. (a) Naked-eye observations of the specimen between the crossed polarizers at the aging period of 1 year [(α)-(γ)] and 1 month [(α')-(γ')], respectively. (b) Typical 2D SAXS patterns from the upper phase and lower phase of each specimen taken after 1 year aging. (c) Radial profiles of the SAXS patterns shown in (b) and SANS profiles. The symbols in black and gray color denote the data of SANS and SAXS, respectively. For curve (v), two SANS profiles taken at different aging period (open circle, 1 day; solid circle, 18 months) demonstrate an influence of the aging time. The indices (i)–(vi) in part (a) are utilized in common to indicate the specimens in the corresponding parts (b) and (c).

scattering patterns in part (b) and the profiles in part (c) are obtained.

Though the physical origin of the two-phase coexistence was not discussed in detail, the previous report [22] assigned the upper and lower phases to the isotropic phase and the LC phase, respectively. In this work internal structures in these two phases were characterized by SANS and SAXS, as described below. The physical origin of the two-phase coexistence also will be discussed in Sec. III B.

The radial SAXS and SANS profiles [Fig. 4(c)] were obtained by a sector or circular averaging of the two-dimensional (2D) patterns, as shown in Fig. 4(b) for SAXS. The sector averaging was carried out on the oriented patterns [Fig. 4(b), (ii), (iv), and (vi)], while the circular averaging was done on the circular ones [Fig. 4(b), (iii) and (v)]. Although the SANS patterns were taken over a larger irradiated volume than the SAXS patterns, they also gave the similar oriented patterns for the lower phases [(ii), (iv), and (vi) in Fig. 4(a)] and the circular one for the upper phases of (iii) and (v).

Each upper phase of specimens (α) to (γ), exhibits a circular 2D scattering pattern [(iii) and (v) in Fig. 4(b)] or hardly any scattering [(i) in Fig. 4(b)], which is consistent with the fact that no macroscopic birefringence can be discerned in the upper phases in Fig. 4(a). Further, the comparison of the radial profiles (iii) and (v) in Fig. 4(c) revealed the fact that the positional correlation among the nanosheets in (v) are more enhanced, giving rise to the broad scattering maxima, than that in (iii), where the scattering intensity monotonically decreases with q according to the power law of $I(q) \sim q^{-2}$, reflecting the scattering from isolated nanosheets as illustrated by the model shown in Fig. 1(b). Generally, the maxima in the profile (v) as well as those in profiles (ii), (iv), and (vi) from the lower phases, shown in Fig. 4(c), reflect the positional order of the sheets along **a**.

The interparticle correlation of the nanosheets for (v) seems anomalously enhanced relatively to that for (iii), despite the fact that SAXS patterns (iii) and (v) commonly show macroscopically random orientation of the sheets. The comparison of the radial profiles (iii) to (v) reveals that the profile (v) is not comparable to the profile (iii) but is comparable to the profile (iv) in the light of the fact that two broad scattering maxima labeled [1] and [2] can be distinguished at nearly the same q values in both of the profiles (iv) and (v). This suggests that the local positional order of the nanosheets in the upper phase (v) is nearly equivalent to that in the lower phase (iv) which shows an extremely anisotropic scattering pattern and hence is reasonably classified as the nematic phase. Then a question is raised as to whether the phase (v) belongs to the nematic phase or the isotropic phase. The situation of the phase (v) that the positional order of the nanosheets is sufficiently developed but

does not end up with the macroscopic orientation may be close to the state (c2) shown in Fig. 1. The broad scattering maxima in profile (v) possibly arise also from either state like (c1) or (c2), where **a**'s take macroscopically random orientation. If the maxima reflect the state (c1) the phase (v) is surely classified into the isotropic phase. If the maxima reflect the state (c2), the phase (v) is classified either the nematic phase (when the grains are large) or the isotropic phase (when the grains are small). Since the irradiated area by x ray $\sim 30\ \mu\mathrm{m}^2$, we anticipate the average grain size of the phase (v) is of order of $\sqrt{30}$ ($\cong 5.5$) μm at maximum [49]. Since the grain size is not large, we assign the phase (v) to the isotropic phase in this paper.

As for the lower anisotropic phase in Fig. 4(b), which commonly shows an extremely high orientational order independent of $\overline{L}$, the degree of the positional order of the $\overline{L} = 0.65$ specimen is clearly different from those of the $\overline{L} = 0.98$ and 12.2 specimens [cf. (ii), (iv), and (vi) of Figs. 4(b) and 4(c)]. The profiles (ii) and (iv) for the $\overline{L} = 12.2$ and 0.98 specimens possess only the two broad scattering maxima marked by ① and ②, hence suggesting the nematic phase, while the profile (vi) for $\overline{L} = 0.65$ has several distinct higher-order peaks and deserves to be defined as the Lay phase.

The difference between the nematic phase and the Lay phase can be described with respect to g factor for the intersheet spacing ($D \equiv D_z$), $g_D = \sigma_D/\overline{D} \equiv \Delta D_{zz}/\overline{D_z}$, where $\sigma_D \equiv \Delta D_{zz}$ is the standard deviation of D. The nematic phase having two scattering peaks is equivalent to $0.12 < g_D < 0.18$. On the contrary, the Lay phase having more than four scattering peaks means that $g_D \leqslant 0.09$ [32].

B. Physical origin of two-phase coexistence

Here we discuss two possible origins for the two-phase coexistence: sedimentation and phase separation. Let us first discuss the sedimentation effect.

1. *Effects of sedimentation*

Since mass density (ρ) of nanosheet ($\rho_{[\mathrm{Nb_6O_{17}}]^{4-}} = 3.16 \times 10^3\ \mathrm{kg/m^3}$) is larger than that of water ($\rho_{\mathrm{H_2O}} = 1.0 \times 10^3\ \mathrm{kg/m^3}$), it is natural to consider that the number density of the nanosheet particles is larger in the lower part of the cell than that in the upper part. This difference brings about the difference in the depolarized light scattering intensity ($\mathrm{H_V}$ or $\mathrm{V_H}$) and hence the transmitted light intensity under the cross-polarizers, denoted hereafter "brightness" for brevity, between the upper and lower parts of the cell. The dilute upper part is expected to have a smaller OC and smaller $\mathrm{H_V}$ scattering intensity than the concentrated lower part, which has a larger OC and $\mathrm{H_V}$ scattering intensity [33].

Let us introduce the gravitational length (l_g), which is given by $l_g = k_B T/(g\Delta\rho d L^2)$ with $\Delta\rho \equiv \rho_{[\mathrm{Nb_6O_{17}}]^{4-}} - \rho_{\mathrm{H_2O}}$ for the individual nanosheets and which defines the decay constant of the local concentration variation of particles (η) with height (h) from the bottom, $\eta(h) = \eta_0 \exp(-h/l_g)$ [50,51], where k_B is the Boltzmann constant, T is the absolute temperature, g is the gravitational acceleration, and η_0 is the concentration of the nanosheets at $h = 0$ (the bottom). Since $\Delta\rho = 2.16 \times 10^3\ \mathrm{kg/m^3}$ is known, l_g depends solely on L at the constant d (= 1.6 nm): $l_g = 8\times10^{-4}$, 0.13, and 0.29 mm for $L =$ 12.2, 098, and 0.65 μm, respectively. This trend of l_g with L contradicts the observed volume fraction of the two phases with $\overline{L}$ as shown in Fig. 4(a): If the particle distribution followed the decay constant l_g, the fraction of the lower bright part would decrease with increasing L; however, the experimental results show the completely opposite trend. Consequently, we can conclude that the sedimentation of individual nanosheet particles is essentially irrelevant to the coexistence of the upper and lower parts.

2. *Effects of phase separation*

Instead, let us consider that each aqueous suspension of the particles at $\phi_\mathrm{p} = 0.01$ inherently has the thermodynamic instability or metastability to form the single phase and thereby undergoes the phase separation into a dilute phase and a concentrated phase. If this is the case, the phase separation develops domains rich and poor in the particles, and these domains are coarsened with time, t. Here it is important to note that the nanosheet suspensions belong to one of typical systems having dynamic asymmetry in which constituent components have a large difference in mobilities [52–55]: The nanosheets have an extremely small mobility compared with water molecules. The phase separation of the dynamically asymmetric systems involves stress diffusion coupling [52,53]. Here the viscoelasticity plays a significant role on phase-separation processes and phase-separated structures. It brings about special characteristics of the so-called viscoelastic phase separation [54–63]. In the viscoelastic phase separation process, the slow component (the nanosheets) tends to form domains rich in the slow component, via the solvent-squeezing mechanism [53–55], which are percolated in 3D space, in the matrix poor in the slow component, even in the case when the slow component has only very small volume fraction, e.g., $\phi_\mathrm{p} = 0.001$ [54] and $\phi_\mathrm{p} = 0.07$ [58].

The characteristic length $\Lambda(t)$ of the percolated domain and its cross-sectional area $A(t)$ increase with time during the coarsening process in order to reduce the interfacial free energy (or the interfacial tension σ) between the domain and the matrix. As the domain grows, $\Lambda(t)$ increases, and as a consequence the gravitational force on the domains (but not on the sheets themselves) ($\sim\frac{4\pi}{3}\Lambda(t)^3\Delta\rho g$) becomes increasingly important against the interfacial tension $\sim 2\pi\Lambda(t)\sigma$. This is because domain rich in the sheets is heavier than the matrix phase poor in the sheets by a factor of $\Delta\rho$. At a critical time, $t_{\mathrm{c,grav}}$, $\Lambda(t = t_{\mathrm{c,grav}})$ increases to Λ_{grav} so that the two forces are balanced, $\Lambda_{\mathrm{grav}} \sim [3\sigma/2(g\Delta\rho)]^{1/2}$. When $t > t_{\mathrm{c,grav}}$ and $\Lambda(t) > \Lambda_{\mathrm{grav}}$, the gravitational force outweighs the interfacial tension and breaks the percolated domain. The broken domains are forced to the lower phase (the concentrated phase rich in the sheets), while the matrix phase is forced to the upper phase (the dilute phase poor in the sheets), resulting in a gravitational-force-induced macroscopic phase separation [64].

Indeed, before reaching the macroscopic two-phase coexistence, we can observe a kind of incubation period, where the dispersions appeared to be macroscopically homogeneous but to show turbidity as a signature of local heterogeneities developed by the phase separation, as shown in parts (α') and (γ') in Fig. 4(a). The period was considerably different among those three specimens. As for the $\overline{L} = 0.98$ specimen, the period is relatively short, and apparently it completed within 1 month, as shown in part (β') in Fig. 4(a) (or even within 1 day,

though the evidence is not shown here). On the other hand, for both $\overline{L} = 12.2$ and 0.65 specimens it took 3 months to observe the macroscopic phase separation into the upper and lower phases. This may infer the following: The thermodynamic driving force for the phase separation increases in the order of $\overline{L} = 0.65$, 0.98, and 12.2, but the mobility of the sheets decreases in the same order; the two opposing physical factors may explain the smallest $t_{c,grav}$ for the $\overline{L} = 0.98$ specimen. The transient existence of the macroscopically single phase as described above also assures the fact that the observed separation into the upper and lower phases is attributed not to the sedimentation but to the phase separation.

An additional remark on the phase-separation behavior of those three $\phi_p = 0.01$ specimens is that not only $\overline{L}$ itself but also g_L may generally play an important role on the phase behavior in conjunction with the effects of fractionation of nanosheets. A significant effect of the fractionation in the particle size on the phase behavior was thoroughly discussed on the "boardlike" goethite (α-FeOOH) colloidal system [65]. The rodlike system showing coexistence of isotropic and smectic phases was found to exhibit the following characteristics: The polydispersity of the particle length in the two phases is nearly the same, while the mean particle length in the isotropic phase is slightly smaller than that in the smectic phase. Such a situation may hold in this study, though its confirmation deserves a future work.

3. *Sedimentation effects as revealed in the upper isotropic phase and lower LC phase*

Recently, van der Beek *et al.* applied the effect of sedimentation to a model platelike colloidal system consisting of gibbsite [$Al(OH)_3$] particles and successfully derived the equilibrium coexistence of more than two phases [23,66]. This phenomenon has been further intensively investigated and established by the research group of Van't Hoff Laboratory at Utrecht University [25,27,65,67]. Contrary to those observations, the present system showed only two-phase coexistence between the upper isotropic and the lower LC phase, which is driven by the phase separation as discussed in the previous section and which is stable for at least a prolonged aging period up to 1 year, and hence no additional phase induced by the sedimentation effect.

The issue remaining to be clarified for the present system is how the sedimentation possibly influences the structure of the upper and lower phases of nanosheet suspensions. The observed effects of the sedimentation on each phase of the nanosheets specimens are summarized in Fig. 5. For the lower phase of the $\overline{L} = 12.2$ specimen aged for 1 year, the circular-averaged SAXS intensity tends to increase with lowering the height position of the sample cell from position 3 to 1 with respect to the fixed incident beam position [Fig. 5(a)]. This indicates that the number density of nanosheets increases with lowering the height position, due to the sedimentation effect. The same tendency was observed on the upper phase of the $\overline{L} = 12.2$ specimen as well as on the both the upper and the lower phases of the $\overline{L} = 0.98$ specimen, though the scattering data are not shown here. This feature can be discerned also by the naked-eye observation through the crossed polarizers. For instance, in the upper phase of the $\overline{L} = 0.98$ specimen [part (iii) of Fig. 4(a) (β)], the bottom area, which is in the vicinity of the phase boundary marked by the arrow, is obviously brighter than the top area, which is indicative of the sedimentation effect.

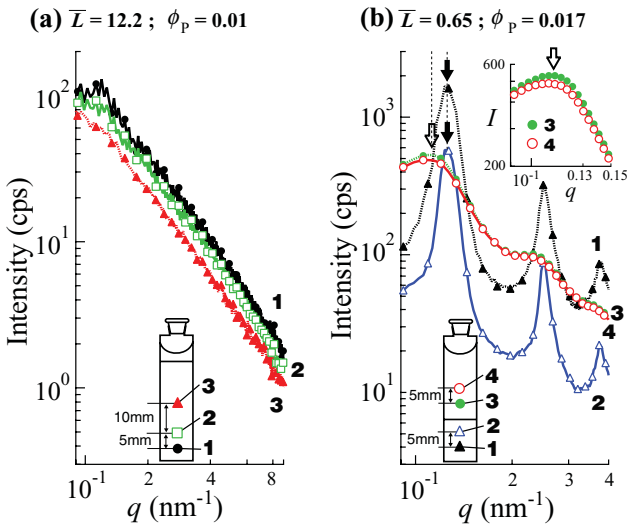

FIG. 5. (Color) Comparison of the circular-averaged scattering profiles taken at different height positions for the specimen of (a) $\overline{L} = 12.2$ and $\phi_p = 0.01$, and (b) $\overline{L} = 0.65$ and $\phi_p = 0.017$. Each scattering profile [labeled 1 to 3 in (a) and 1 to 4 in (b)] was obtained at the corresponding height position shown in the inset to (a) and (b). For the sake of clarity, in (b) the solid and open arrows designate the positions of the first-order scattering maximum on the profiles of the LC phase and the isotropic phase, respectively. The inset to (b) highlights the profile around the first-order maximum for the isotropic phase.

Figure 5(b) shows the circular-averaged scattering profiles of the $\overline{L} = 0.65$ specimen taken at positions 3 and 4 in the upper phase and at positions 1 and 2 in the lower phase. Here the following points are worth noting; (1) The peak position of the isotropic phase shown by the open arrow and that of LC phase shown by solid arrows are nearly independent of the height position, although (2) the scattering intensity obviously increases with lowering the height position. (3) The peak position of the LC phase is smaller than that of the isotropic phase. This fact (1) suggests that the sedimentation within each phase does not influence the characteristic spacing of the nanosheets, in a clear contrast to the sedimentation effect on the colloidal dispersion consisting of gibbsite particles [25] where an obvious decrement in the intercolumnar spacing by ca. 8 nm was observed upon lowering the height position of the sample by 5 mm (cf. Fig. 4 in Ref. [25]). The fact (2) suggests that the sedimentation effect influences number of the sheets in the stack formed by the sheets; the lower the height position is, the higher is the number. The fact (3) suggests that the lower LC phase has a larger ϕ_p than the upper isotropic phase. This fact is considered to reflect the phase separation into the phase having the larger ϕ_p and the phase having the smaller ϕ_p.

Although it is beyond the scope of this study to elucidate the origin of the above discrepancies in the structures of the colloidal suspensions between nanosheets and gibbsite particles with respect to the fact (1) described above, we can point out that there are a variety of differences in the experimental conditions between the reported works [23,25,27,65–67] and

the present work. For instance, the differences in (i) ϕ_p, (ii) the particle shape and size, and (iii) the effective charge density or κ^{-1} are likely the factors which brought about the differences in the sedimentation effects and phase separation behavior. To clarify the effect of each factor deserves a future work.

C. Concentration dependence at fixed $\overline{L} = 0.65$: Remarkable concentration fluctuations of the nanosheets in the LC phase

1. Concentration dependence of dispersions

The circular-averaged SAXS scattered intensity $I(q)$, 2D patterns, and structure factors, $S(q)$, taken at various ϕ_p in the range of 0.01 to 0.037 for the $\overline{L} = 0.65$ specimen were shown in Figs. 6(a)–6(e). In Fig. 6(c), typical 2D scattering patterns obtained from each suspension are placed from top to bottom in order of increasing ϕ_p. Furthermore, for the specimens in the coexisting phase, the scattering patterns from upper phase and lower phase are placed at the left side and the right side, respectively. Judging from a common feature of a circular pattern found for patterns (1) to (5) in Fig. 6(c) as well as a few broad maxima on $S(q)$'s in Fig. 6(e) obtained from patterns (1) to (5) in Fig. 6(c), which suggests a liquidlike order of nanosheets, the phases numbered (1)–(5) were identified as the isotropic phase. On the other hand, due to another common feature of a preferential orientation, patterns (6) to (10) in Fig. 6(c) as well as the sharp higher-order peaks on $S(q)$'s in Fig. 6(d) obtained from patterns (6) to (10), the phases corresponding to (6)–(10) should be classified to the same Lay phase.

According to the results shown in Fig. 4, the $\overline{L} = 0.65$ suspensions having $\phi_p \geqslant 0.01$ are expected to form the isotropic/Lay coexisting phase or an anisotropic Lay single phase. However, as shown in scattering patterns (1) and (2) in Fig. 6(c), only the isotropic single phase was observed for the $\phi_p = 0.01$ and 0.0125 suspensions. This discrepancy can be attributed to a shortage of the aging period (3 weeks) for the specimens used to obtain the data in Fig. 6. The $\overline{L} = 0.65$ specimen used in Fig. 4 also kept a single phase, when its aging period is shorter than 3 months, as demonstrated in part (γ') in Fig. 4(a). In any case, once an anisotropic scattering pattern appeared in the $\overline{L} = 0.65$ suspensions ($\phi_p \geqslant 0.017$) either in the lower phase [patterns (6)–(8) in Fig. 6(c)] or in the monophase [patterns (9) and (10) in Fig. 6(c)], it exhibits multiple order scattering peaks [cf. (6)–(10) in Figs. 6(b) and 6(d)], indicative of an extremely high positional order, so that the phase can be identified as the Lay phase. As there is no experimental evidence about the positional order along the lateral direction of the sheets at the moment, it is impossible to further identify whether the Lay phase of the $\overline{L} = 0.65$ specimen belongs to the lamellar phase or the SCN phase.

2. Concentration fluctuations of the nanosheets in the LC phase

Another structural datum obtained from the scattering profile is the spacing $\overline{D}$, which is determined by $\overline{D} = 2\pi/q_m$. Here q_m denotes the q value at the first-order peak. In Fig. 7, $\overline{D}$ for the $\overline{L} = 0.65$ suspensions is plotted as a function of ϕ_p in the double logarithmic scale. To estimate the $\overline{D}$ value correctly as much as possible, the influence of gravity as well as that of aging period on the q_m value was taken into account as follows. Concerning the gravity effect, the dependence of

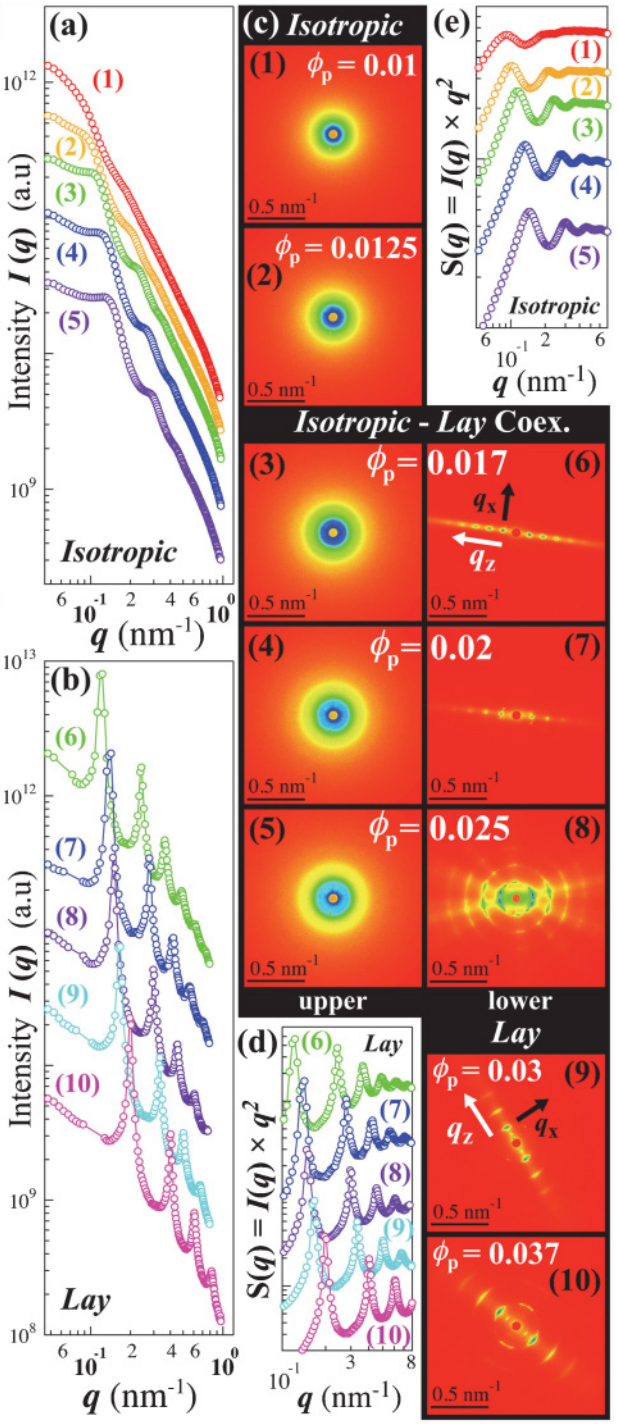

FIG. 6. (Color) ϕ_p dependence of the $\overline{L} = 0.65$ specimen at the aging period of 3 weeks; the radial profiles shown in parts (a) and (b) are obtained after circular averaging the 2D SAXS patterns shown in Fig. 6(c). (c) 2D SAXS patterns obtained from the specimens of various ϕ_p from 0.01 to 0.037. The specimens of $\phi_p = 0.01$ and 0.0125 exhibited only the isotropic single phase, and those of $\phi_p = 0.03$ and 0.037 showed only the oriented Lay single phase, while those of $\phi_p = 0.017$, 0.02, and 0.025 presented the coexistence of the isotropic and oriented Lay phases. (d) and (e) are structure factors, $S(q) = q^2 I(q)$, obtained from the radial profiles shown in Figs. 6(b) and 6(a), respectively. Throughout Figs. 6(a)–6(e) the running numbers (1)–(10) are utilized in common to indicate the correspondence of the patterns and the profiles.

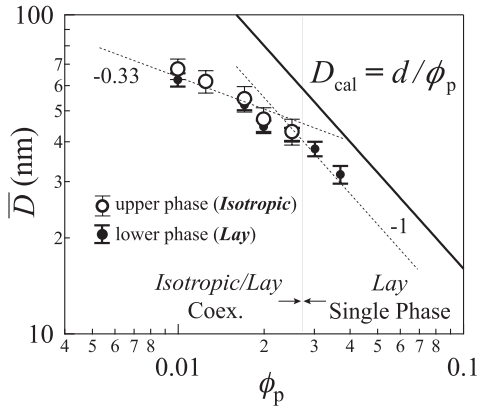

FIG. 7. ϕ_p dependence of $\overline{D}$ for the nanosheet specimens of $\overline{L} = 0.65$. The $\overline{D}$ values were estimated based on the data of Fig. 6(c), except for $\overline{D}$ for the lower phase at the $\phi_p = 0.01$ specimen; the $\overline{D}$ value for the lower phase at $\phi_p = 0.01$ was estimated from the pattern (vi) in Fig. 4(b). The variation of $\overline{D}$ with the height position as well as the aging period of the specimen is included within the error bars (see the text). The open circles with thin error bars are the data of the upper isotropic phase and the solid circles with thick error bars are the data of the lower Lay phase. The solid line represents a calculated D value (see the text).

$\overline{D}$ value on the height position of the cell was inspected by scanning over several millimeters at every 100 μm height with the SAXS measurements. The results revealed that the range of the fluctuations in $\overline{D}$ with height within both the isotropic phase ($< \sim$5 nm) and the Lay phase ($< \sim$5 nm) is much smaller than the change in $\overline{D}$ itself (68–31 nm) with ϕ_p (0.01–0.037), as partially demonstrated in Fig. 5(b). Hence, the gravity effect was proved insignificant. The repeated measurements at different aging periods ranging from 1 day to more than 1 year [cf. profiles (v) with open and solid circles in Fig. 4(c)] revealed that the major change in $\overline{D}$ occurred within 1 day, and $\overline{D}$ kept constant within the fluctuations of a few nm after 1 day. Those experimental pieces of evidence indicate that thermal equilibrium in the length scale of $\overline{D}$ can be practically attained within the time scale of a day, though phase equilibria in a macroscale can be reached only after an extremely long period [cf. Fig. 4(a)].

Then the following trends are deduced from Fig. 7: (a) $\overline{D}$ generally decreases with increasing ϕ_p and this tendency holds even in the isotropic/Lay coexistence region ($0.01 \leqslant \phi_p \leqslant 0.025$); (b) In the isotropic/Lay coexisting phase, the $\overline{D}$ value of each phase at a given ϕ_p is nearly identical, that is, $\overline{D}_{isotropic} \sim \overline{D}_{Lay}$; (c) the ϕ_p dependence of $\overline{D}$ is different between the isotropic/Lay coexistence region (i.e., $0.01 \leqslant \phi_p \leqslant 0.025$) and Lay single phase region ($\phi_p > 0.025$). In the latter case, $\overline{D}_{Lay} \sim \phi_p^{-1}$, and this ϕ_p dependence can be derived from a simple assumption as described below. Trends (a) and (b) described above are intuitively against the normal lever rule applicable to an ordinary coexisting two phases, in which the following behaviors are anticipated for $\overline{D}$: (1) $\overline{D}_{isotropic} > \overline{D}_{Lay}$; (2) $\overline{D}_{isotropic} \sim \phi_p{}^0$ and $\overline{D}_{Lay} \sim \phi_p{}^0$, independent of ϕ_p, though the volume fraction of those two phases is varied with ϕ_p.

Another remarkable trend in Fig. 7 is that (d) the measured $\overline{D}$ value is much smaller than the calculated one, $D_{cal} = d/\phi_p$ derived on the basis of the assumption of a uniform 1D swelling of nanosheet particles with water, as shown by the solid line in Fig. 7. Consequently the spatial concentration fluctuations of nanosheets is crucial to account for the discrepancy between the observed and calculated results. That is, in both the upper isotropic and the lower Lay phases, as well as in the Lay single phase, the obtained $\overline{D}$ value from the scattering profile may reflect only the local concentration in grains, where the nanosheets are self-assembled more densely than the bulk (average) concentration, and these grains coexist with the nanosheet-poor matrix. It is important to note that this finding further verifies firmly our previous observation of the intriguing concentration fluctuations of the sheets observed in the Lay single phase [1]. It is noteworthy that the grain or cluster formation of the colloidal particles has been directly observed by optical microscopy in some other systems too [54,55,68–71]. The following argument can be deduced for the amplitude of the concentration fluctuations. As for the average (or bulk) concentration of nanosheets, $\phi_{p\,isotropic} < \phi_{p\,Lay}$ is expected, since the isotropic phase locates the upper part of the cell. While trend (b) assures that the local concentration of the sheets within the grains rich-in the sheets in the isotropic phase, $\phi_{p\,isotropic,local}$, is almost equivalent to that in the Lay phase, $\phi_{p\,Lay,local}$. Consequently, the following relation is given for the amplitude of local concentration fluctuations of the sheets in the jth phase (j = isotropic or Lay), $\Delta\phi_{pj} \equiv \phi_{pj,local} - \phi_{pj}$ (ϕ_{pj} being the bulk concentration of the sheets in the jth phase); $\Delta\phi_{p\,isotropic} > \Delta\phi_{p\,Lay}$. This conclusion is consistent with the thermodynamic principle that the osmotic compressibility is decreased with increasing ϕ_p. Furthermore, the suppression of the difference between D_{cal} and measured $\overline{D}$ value with increasing ϕ_p is rationalized by the same principle.

It is worth noting that trend (b) was observed only for the $\overline{L} = 0.65$ specimens, for which the upper phase is depicted by Fig. 1(c) and the lower phase is depicted by 1(e) or 1(f). However, for the $\overline{L} = 0.98$ and 12.2 ($\phi_p = 0.01$) specimens the phase separation occurred between the phases corresponding to Figs. 1(b) and 1(d), and hence $\overline{D}_{isotropic}$ for the gaslike upper phase was not determined from the scattering experiment. On the other hand, the $\overline{D}$ values of the lower phase ($\overline{D}_{nematic}$) were measured to be $\sim$78.5nm ($q_m \sim 0.08$ nm^{-1}) and $\sim$97 nm($q_m \sim 0.065$ nm^{-1}) for the $\overline{L} = 0.98$ and 12.2 ($\phi_p = 0.01$) specimens, respectively. The obtained $\overline{D}_{nematic}$ seems still smaller than D_{cal}. For instance, in the case of $\overline{L} = 12.2$ ($\phi_p = 0.01$), $D_{cal} = d/\phi_{p\,nematic} \sim \frac{1.6}{0.01/(9/10)} = 145$ nm [72], and thus $\overline{D}_{nematic}/D_{cal} = 97/145 \sim 0.7$, suggesting that nearly 30% of water inside of the nematic phase does not take part in the uniform swelling of the sheets but contributes to produce the local concentration fluctuations of the sheets.

A crucial question remaining in conjunction with Fig. 7 is how the equilibrium $\overline{D}$ in the grains rich in nanosheets is predicted in the isotropic phase and in the Lay phase. To predict the LC phase, the shape anisotropy of the particles is crucial, and the hard-core potential is still acceptable [4,73,74], while to predict a spacing, the notion of the potential minimum should be significant. In this context, the "secondary minimum," which appeared in the Derjaguin-Landau-Verwey-Overbeek (DLVO) theory [75,76], can be applicable to the current system, though recent progress in theories has proposed

some modifications to take into account Coulombic attractive interactions between like-charged colloidal particles [77–80]. Below, we attempt to explain our experimental results in the context of the DLVO theory, where the term of van der Waals interactions is arisen from a set of charged thin plates oriented parallel to each other in water medium [81]. The pairwise free energy potential (hereafter denoted as F_{DLVO}) per two parallel plates is a function of valence of the counterions (z), dielectric constant of the medium (ε), Hamaker constant (A), electric potential at the surface of the plate (ψ_0), n, T, and the particle size (L and d). F_{DLVO} is calculated for relatively low n values (1.6–3.2×10^{-4} mol/L), with fixing the other parameters as follows: $z=+1$, $\varepsilon = 78\varepsilon_0$ F/m (i.e., assuming water), where ε_0 is vacuum permittivity, $A = 1.81\times10^{-19}$ J, $\psi_0 = -40$ mV, $T = 300$ K, $L = 0.65$ μm, and $d = 1.6$ nm. As the results, the potential minimum of F_{DLVO} is located at 64 (with $F_{\mathrm{DLVO}} = -0.26\,k_BT$), 46 ($F_{\mathrm{DLVO}} = -0.83\,k_BT$), and 32 nm ($F_{\mathrm{DLVO}} = -2.90\,k_BT$) for $n = 1.6\times10^{-4}$, 2.3×10^{-4} and 3.2×10^{-4} mol/L, respectively. Those calculation results indicate that a slight increase in n brings a considerable decrease in equilibrium $\overline{D}$, and each value of 64, 46, and 32 nm is close to the measured $\overline{D}$ value on the $\phi_{\mathrm{p}} = 0.01$ ($\overline{D}_{\mathrm{isotropic}} = 67.7$ nm; $\overline{D}_{\mathrm{Lay}} = 62.6$ nm), 0.02 ($\overline{D}_{\mathrm{isotropic}} = 47.1$ nm; $\overline{D}_{\mathrm{Lay}} = 44.6$ nm), and 0.037 ($\overline{D}_{\mathrm{Lay}} = 31.6$ nm) specimens, respectively. Thus, the message from the above calculations is that the classical DLVO theory can rationalize a general $\overline{D}$ behavior shown in Fig. 7, provided an effective increase in n (consisting of both K^+ and $C_3H_7NH_3^+$) from 1.6×10^{-4} to 3.2×10^{-4} mol/L is produced with increasing of ϕ_{p} from 0.01 to 0.037.

3. *Caillé's line shape analysis*

Caillé's line shape analysis has been applied to analyze the dynamics of the lamellar phase [82–90]. We believe that the analysis can be applied to the Lay phase also. However, it is important to note the following limitations in the line shape analysis of this phase based on the SAXS. The length scale covered by SAXS ($\leqslant$100 nm) is much less than the average lateral size of the sheet $\overline{L}$, for example, 650 nm in the case of the $\overline{L} =$ 0.65 specimen. As a consequence, the analysis is limited to the undulation modes within the sheets themselves and the modes relevant to ΔD_{zz} in the direction perpendicular and parallel to **a**, respectively. We are not able to analyze large-length scale intersheet undulation modes involving the length scale larger than $\overline{L}$ (or generally $\overline{D_x}$ and $\overline{D_y}$) in the x-y plane (Fig. 2).

Experimentally, with a careful observation on the SAXS patterns of the Lay phase at different ϕ_{p}, as shown in patterns (6)–(10) in Fig. 6(c), we can categorize those patterns into two types: One is common to patterns (6) and (7), both of which arise from the Lay phase coexisting with the isotropic phase, exhibiting several diffraction spots having nearly a circular shape; the other is common to patterns (9) and (10), both of which arise from the Lay single phase, exhibiting the diffraction spots elongated along the q_x direction, the direction of which is defined in patterns (6) and (9). The results obtained from Caillé's analysis for these two kinds of the typical scattering patterns [pattern (6) and (9) for $\phi_{\mathrm{p}} =$ 0.017 and 0.03, respectively] will be useful to clarify the dynamics of the nanosheets in the Lay phase.

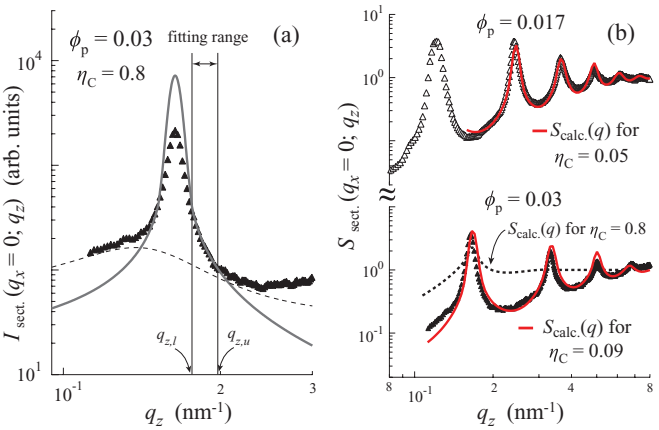

FIG. 8. (Color) Line shape analysis for two $\overline{L} = 0.65$ specimens ($\phi_{\mathrm{p}} = 0.017$ and 0.03) in the Lay phase. (a) Comparison of the experimental scattering function $I_{\mathrm{sect.}}(q_x = 0; q_z)$ (solid triangles) with the Caillé's function (thick gray line) ($|q_z - q_{z\mathrm{m},1}|^{-P}$ with $P = 2 - \eta_{\mathrm{C}}$) for the specimen with $\phi_{\mathrm{p}} = 0.03$. (b) $S_{\mathrm{sect.}}(q_x = 0; q_z)$ for the experimental scattering profiles (triangles) were compared with the theoretical ones [$S_{\mathrm{calc.}}(q_x = 0; q_z)$; see the text]. For the $\phi_{\mathrm{p}} =$ 0.03 specimen $S_{\mathrm{calc.}}(q_x = 0; q_z)$ was carried out for two η_{C} values, 0.09 (solid red line) and 0.8 (broken line).

The line shape of the first-order peak of $I_{\mathrm{sect.}}(q_x = 0; q_z)$, which is obtained by sector-averaging scattering pattern (9) in Fig. 6(c) over 5° from −2.5° to +2.5° with respect to the direction of the preferential orientation of the pattern (designated by q_z), is compared with the Caillé's theoretical function given by the power law, $I(q_x = 0; q_z) \propto |q_z - q_{z\mathrm{m},1}|^{-P}$, with $P = 2 - \eta_{\mathrm{C}}$ [82] in Fig. 8(a). Here $q_{z\mathrm{m},1}$ denotes the q_z value at the first-order peak and the parameter η_{C} is related to the elastic moduli of the phase given by $\eta_{\mathrm{C}} = \frac{q_{z\mathrm{m},1}^2 k_B T}{8\pi\sqrt{BK}}$ with B and K being the compression modulus and the curvature modulus, respectively, of the layered structure.

Since the experimentally obtained $I_{\mathrm{sect.}}(q_x = 0; q_z)$ shown by triangles in Fig. 8(a) is smeared by the resolution function of the SAXS apparatus, the theoretical function of $|q_z - q_{z\mathrm{m},1}|^{-P}$ also was smeared with the same resolution function for a fair comparison between theoretical $I(q_x = 0; q_z)$ and experimental $I_{\mathrm{sect.}}(q_x = 0; q_z)$. The best fit of the smeared theoretical function (thick solid line) with the experimental function was conducted only for the specimen with $\phi_{\mathrm{p}} = 0.03$. The reason why the same analysis was not conducted for the specimen with $\phi_{\mathrm{p}} = 0.017$ is discussed later in conjunction with Fig. 9(a). The result gives $\eta_{\mathrm{C}} = 0.8$, where the q_z range used for the fitting was indicated by the vertical solid lines, drawn at $q_z = q_{z,l}$ and $q_{z,u}$, on the basis of the following criteria. (1) The theoretical scattering function diverges to infinity at $q_z = q_{z\mathrm{m},1}$, while the experimental scattering function does not; hence, the two functions naturally do not agree at q_z close to $q_{z\mathrm{m},1}$, that is, $|q_z - q_{z\mathrm{m},1}| < q_{z,l}$. (2) The experimental first-order scattering peak seems to be accompanied by a broad scattering maximum or shoulder or a background scattering as illustrated by the broken line for only a visual guide in Fig. 8(a) and hence it deviates from the theoretical function at $|q_z - q_{z\mathrm{m},1}| > q_{z,u}$. The scattering functions were further examined by the analysis involving a whole shape of the experimentally obtained profile,

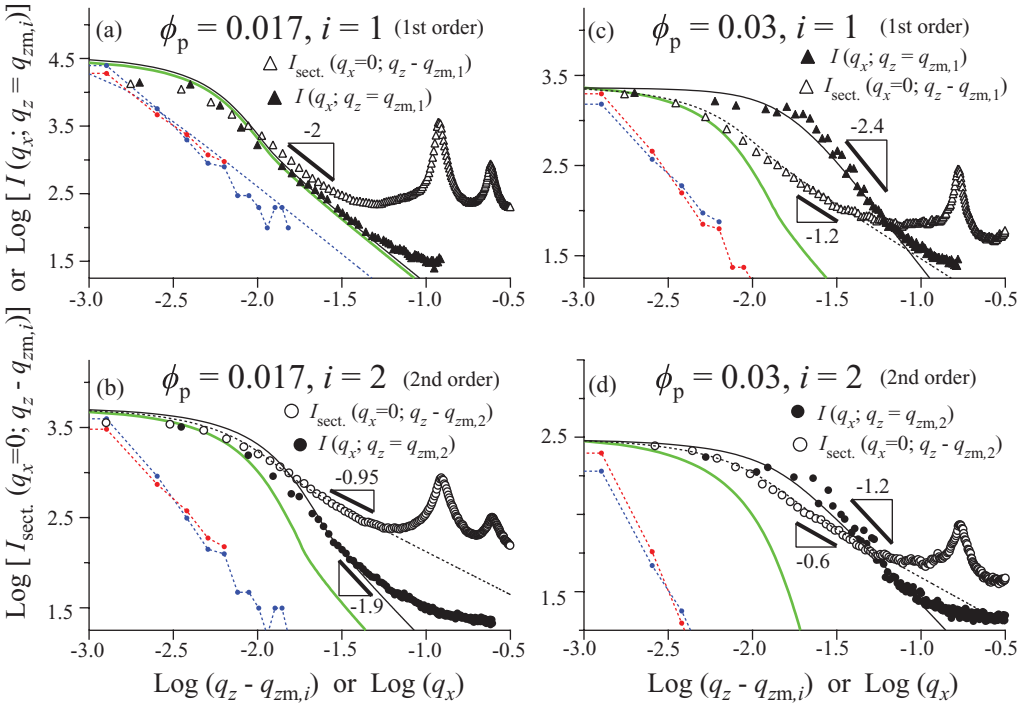

FIG. 9. (Color) Line shapes of the first- and second-order peaks were examined with $I_{sect.}(q_x = 0; q_z - q_{zm,i})$ and $I(q_x; q_z = q_{zm,i})$ profiles for the $\phi_p = 0.017$ specimen in parts (a) and (b), respectively, and the $\phi_p = 0.03$ specimen in parts (c) and (d), respectively. In Figs. 9(a)–9(d), the solid and dotted black lines are the smeared Caillé's functions of $|q_x|^{-P'}$ and $|q_z - q_{zm,i}|^{-P}$ with the relation of $P' = 2P$ and $P = 2 - i^2\eta_C$. The red and blue circles with broken lines represent the profiles of the measured direct beam along the q_x and q_z directions, while the green thick solid line represents the estimation of the rocking curve of the direct beam (or the instrumental resolution function). The base of the logarithm is 10.

concerning not only of the first-order maximum but also the higher-order maxima, with the theoretical function presented by Nallet *et al.* [88].

Experimentally obtained $S_{sect.}(q_x = 0; q_z)$ for both $\phi_p = 0.017$ and $\phi_p = 0.03$ specimens, which are the structure factors $I_{sect.}(q_x = 0; q_z){q_z}^2$, over the q range of nearly one decade (open and solid triangles for the $\phi_p = 0.017$ and $\phi_p = 0.03$ specimens, respectively) are compared with the calculated structure factors [$S_{calc.}(q_x = 0; q_z)$, the red solid line] in Fig. 8(b). Here a model of finite number of the stacked layers (N) possessing Gaussian variables of correlation function is assumed:

$$S_{calc.}(q_x = 0; q_z) = 1 + 2\sum_1^{N-1}\left(1 - \frac{i}{N}\right)\cos(iq_z\overline{D}) \times \exp\left[-\frac{q_z^2}{2}\langle(u_i - u_0)^2\rangle\right]$$

where $\langle(u_i - u_0)^2\rangle$ is given by Caillé's formula, $\langle(u_i - u_0)^2\rangle = \frac{\eta_C}{2\pi^2}[\ln(\pi i) + \gamma]\overline{D}^2$, and γ is Euler's constant. This $S_{calc.}(q_x = 0; q_z)$ function is further convoluted with the resolution function of the apparatus and compared with $S_{sect.}(q_x = 0; q_z)$. In the calculation of $S_{calc.}(q_x = 0; q_z)$, N was calculated to be 108 and 147 for the specimens of $\phi_p = 0.017$ and $\phi_p = 0.03$, respectively, by assuming that the product of $N\overline{D}$ will be comparable to the diameter of irradiated x-ray beam (~5.5 μm), where $\overline{D}$ was measured to be 51 nm for $\phi_p = 0.017$ and 37.5 nm for $\phi_p = 0.03$ by SAXS. Hence, the adjustable parameter to fit $S_{calc.}(q_x = 0; q_z)$ with $S_{sect.}(q_x = 0; q_z)$ is only η_C. Note here for the $\phi_p = 0.017$ specimen that the fitting was conducted by weighting of only the second- and higher-order peaks, because the first-order peak should be ignored due to the problem to be discussed later in conjunction with Fig. 9(a). A reasonable agreement between $S_{sect.}(q_x = 0; q_z)$ and $S_{calc.}(q_x = 0; q_z)$ was obtained for $\eta_C = 0.05$ for the $\phi_p = 0.017$ specimen and $\eta_C = 0.09$ for the $\phi_p = 0.03$ specimen. The η_C values thus obtained by the two types of the analyses in Figs. 8(a) and 8(b) for the $\phi_p = 0.03$ specimen did not agree. In the case of the $\phi_p = 0.03$ specimen, $S_{calc.}(q_x = 0; q_z)$ obtained by assuming $\eta_C = 0.8$ is given by the thick dotted line. The $S_{calc.}(q_x = 0; q_z)$ for $\eta_C = 0.8$ does not fit at all with $S_{sect.}(q_z)$, implying that the analysis in Fig. 8(a) for $\phi_p = 0.03$ based on Caillé's analysis overestimated η_C for the reason to be discussed below.

The origin of overestimation of η_C value on the analysis of Fig. 8(a) may be due to the broadening of the experimental first-order scattering maximum shown in Fig. 8(a) which is attributed to the following two reasons as described in the preceding paragraph. (1) the finite number of N, which broadens the peak in the q_z range satisfying $|q_z - q_{zm,1}| < q_{z,l}$, and (2) the background scattering, which broadens the peak in the q_z range satisfying $|q_z - q_{zm,1}| > q_{z,l}$. The Caillé's theory does not account for the physical factors (1) and (2), while the theory by Nallet *et al.* accounts for factor (1). The physical factor (2) may be due to the remarkable concentration fluctuations of nanosheets, which has been already discussed in Sec. III C2. The nanosheet dispersions contain the grains in which the nanosheets are more densely and regularly packed than the matrix phase in which the nanosheets are less densely and less regularly packed. The grains and the matrix give

rise to the sharp scattering maxima and the broad background scattering (as illustrated by the broken line), respectively. Taking those physical factors into account, the formula of Nallet *et al.* [88], which takes into account the finite N, is more suitable than Caillé's analysis [82] in order to deduce a reliable η_C value from the scattering profile of the nanosheet specimens.

The η_C value ~0.09 for the $\phi_p = 0.03$ specimen is very small compared with those obtained from the lamellar phase composed of rodlike octyloxy-cyanobiphenyl molecules (η_C in the range of 0.17–0.38) [83] or surfactant/solvent membranes ($\eta_C \geqslant 0.13$) [85,86,88]. This is indicative of a fairly rigid property of nanosheet layers in comparison to the lamellar phase composed of small molecules as described above. The high rigidity of the nanosheets seems reasonable in light of (i) the nanosheet being built up by the covalently bonded atoms and in light of (ii) those charged layers interacting with each other under the condition of the low ionic strength (n).

Some additional aspects on the line shape anisotropy with respect to the q_x and q_z directions are worth mentioning, since only a limited number of previous SAXS studies [87,91] went into the detailed discussion on this issue. On the theoretical side, the Caillé's formula predicts the asymptotic q behavior, $I(q_x; q_z = q_{zm,1}) \sim |q_x|^{-P'}$ ($P' = 4 - 2\eta_C = 2P$), for the first-order peak appearing in the direction q_x perpendicular to the layer stacking or parallel to the layer surfaces, the direction of which is defined by the black arrow in Fig. 6(c) (6) and (9). The anisotropic decay is further generalized for the ith-order scattering peak $I(q_x; q_z = q_{zm,i}) \sim |q_x|^{-P'}$ and $I_{sect.}(q_x = 0; q_z - q_{zm,i}) \sim |q_z - q_{zm,i}|^{-P}$, with the relation of $P' = 2P$ and $P = 2 - i^2\eta_C$, where $q_{zm,i}$ denotes the q_z value at the ith-order peak [84].

The line shape observed on the $I_{sect.}(q_x = 0; q_z - q_{zm,1})$ and $I(q_x; q_z = q_{zm,1})$ for the first-order peak of the $\phi_p = 0.017$ specimen in Fig. 9(a) are nearly the same, which is thought to be due to the fact that the scattering peak possibly reflects the shape of direct beam profile itself. The measured direct beam, whose profiles along the q_x and q_z directions are shown by red and blue circles with dotted lines, respectively, possesses a sufficiently narrow width as compared with those of scattering peaks from specimens. However, after taking the effects of the divergence of the wavelength of incident x-ray (~2%) and the spatial resolution of the detector into account, the net apparatus resolution function is broadened to the thick solid green curve. Hence, it was proven in the case of the first-order peak of the $\phi_p = 0.017$ specimen that the real $I_{sect.}(q_x = 0; q_z - q_{zm,1})$ and $I(q_x; q_z = q_{zm,1})$ profiles are certainly hidden by the apparatus resolution function. This is the reason why the first-order peak was not applied to the line shape analysis for the specimen with $\phi_p = 0.017$ in Figs. 8(a) and 8(b).

The anisotropic decay of the peak intensity with q_x (>0) and q_z - $q_{zm,i}$ (>0) (i = 1 or 2) was actually observed on the second-order peak of the $\phi_p = 0.017$ specimen [Fig. 9(b)], as well as on the first- and second-order peaks of the $\phi_p = 0.03$ specimen shown in Figs. 9(c) and 9(d), respectively. Among those profiles the power exponent P' observed on the profile $I(q_x; q_z = q_{zm,i})$ with q_x is certainly larger than that P observed on the profile $I_{sect.}(q_x = 0; q_z - q_{zm,i})$ with $|q_z - q_{zm,i}|$ by a factor of 2, in accordance with the prediction by Caillé ($P' = 2P$), although the η_C values estimated from the power exponents were too large, $\eta_C = 0.26$ for $\phi_p = 0.017$ and 0.8 (the first-order peak) or 0.35 (the second-order peak) for $\phi_p = 0.03$, mainly due to neglect of the effect of the finite N, as already pointed out.

Thus, the anisotropic decay of the scattering function with the scattering vector $\boldsymbol{q}$ as characterized by $P' \sim 2P$ is inferred, concerning the line shape inherent in the Lay phase of the $\overline{L} = 0.65$ specimens, commonly for the two kinds of the scattering patterns. Thus, it turns out that the apparent difference in the shape anisotropy of the diffraction spots for the two kinds of the patterns simply reflects the difference in the values of $P' = 2P$: A small increase of P with ϕ_p gives rise to a large increase of P', hence accounting for the larger shape anisotropy of the diffraction spots in the $\phi_p = 0.03$ specimen than in the $\phi_p = 0.017$ specimen. However, the origin of the increment of the peak width or the value η_C with ϕ_p in $I(q_x; q_z = q_{zm,i})$ is not clarified here and hence is left for a future work.

IV. SUMMARY

This study has elucidated the following three intriguing behaviors in the lyotropic LC system composed of charged sheetlike particles having a very large shape anisotropy. The first one is that the observed LC phase sharply changed from the nematic phase to the layered phase with reducing the average lateral size ($\overline{L}$) of the particles below 1 μm at the constant concentration of the particles $\phi_p = 0.01$, keeping the two-phase (isotopic and LC phases) coexistence. What is surprising on this change should be further stressed as follows: The difference between the specimens forming nematic and layered phases (defined as Lay phase) involves only the slight change in $\overline{L}$, though both specimens have a considerable polydispersity in their lateral size. Nevertheless, in the Lay phase, the regularity of the interparticle spacing (D) is high enough to show the g_D factor, which represents the normalized standard deviation of D ($\sigma_D/\overline{D}$), being $g_D <$ 0.09, while in the nematic phase $0.12 < g_D < 0.18$.

The second one is related to the average D values ($\overline{D}$) in the Lay-isotropic phase coexisting specimens: At a given ϕ_p, the $\overline{D}$ in the Lay phase was almost identical to that in the isotropic phase. This implies a larger concentration of fluctuations in the isotropic phase than in the Lay phase. The concentration fluctuations are brought about by formation of grains rich in the particles in the matrix poor in the particles. The ϕ_p dependence of $\overline{D}$ was different between the ϕ_p range for the two-phase coexisting phase ($\overline{D} \sim \phi_p^{-1/3}$) and that for the single Lay phase ($\overline{D} \sim \phi_p^{-1}$). The observed $\overline{D}$ in both ϕ_p ranges were smaller than the predicted D values calculated by the uniform 1D swelling of the particles in water. These findings also indicate that the large concentration fluctuations in the isotropic and Lay phases and that the concentration fluctuations are different for the two ϕ_p ranges. The concentration fluctuations found in the Lay phase firmly supports our previous finding [1] that the domains poor in the particles are spatially distributed with a mass fractal structure.

The third one is the physical origin of the two-phase coexistence. We found that the two-phase structures arise from phase separation of the charged particles from water which

were nondeliberately brought about in the thermodynamic metastable or unstable state in our experimental condition. We propose that the macroscopic phase separation is assisted by the gravitational force which effectively acts on the phase-separated domains exceeding the critical size, Λ_{grav}, as detailed in the text.

ACKNOWLEDGMENT

The synchrotron radiation (SAXS) experiments were performed at the BL40XU in the SPring-8 with the approval of the Japan Synchrotron Radiation Research Institute (JASRI) (Proposal No. 2009A1572).

[1] D. Yamaguchi, N. Miyamoto, S. Koizumi, T. Nakato, and T. Hashimoto, J. Appl. Crystallogr. **40**, s101 (2007).
[2] S. Chandrasekhar, *Liquid Crystals*, 2nd ed. (Cambridge University Press, Cambridge, 1992).
[3] P. G. de Gennes and J. Prost, *The Physics of Liquid Crystals*, 2nd ed. (Oxford University Press, Oxford, 1993).
[4] L. Onsager, Ann. N.Y. Acad. Sci. **51**, 627 (1949).
[5] See, e.g., G. J. Vroege and H. N. W. Lekkerkerker, Rep. Prog. Phys. **55**, 1241 (1992).
[6] R. Eppenga and D. Frenkel, Mol. Phys. **52**, 1303 (1984).
[7] D. Frenkel and B. M. Mulder, Mol. Phys. **55**, 1171 (1985).
[8] D. Frenkel, Liq. Cryst. **5**, 929 (1989).
[9] M. P. Allen, Phys. Rev. Lett. **65**, 2881 (1990).
[10] Note here that the solid phase can be generally defined as the one in which the colloidal particles form a three-dimensional lattice with a long-range order in the matrix media.
[11] J. A. C. Veerman and D. Frenkel, Phys. Rev. A **45**, 5632 (1992).
[12] M. A. Bates and D. Frenkel, J. Chem. Phys. **110**, 6553 (1999).
[13] M. A. Bates and D. Frenkel, J. Chem. Phys. **111**, 1732 (1999).
[14] H. Zocher, Z. Anorg. Allg. Chem. **147**, 91 (1925).
[15] I. Langmuir, J. Chem. Phys. **6**, 873 (1938).
[16] S. Hachisu and K. Furusawa, Science Light, **12**, 157 (1963).
[17] J. C. P. Gabriel, C. Sanchez, and P. Davidson, J. Phys. Chem. **100**, 11139 (1996).
[18] F. M. van der Kooij and H. N. M. Lekkerkerker, J. Phys. Chem., B **102**, 7829 (1998).
[19] A. B. D. Brown, C. Ferrero, T. Narayanan, and A. R. Rennie, Eur. Phys. J. B **11**, 481 (1999).
[20] F. M. van der Kooij, K. Kassapidou, and H. N. M. Lekkerkerker, Nature (London) **406**, 868 (2000).
[21] J. C. P. Gabriel, F. Camerel, B. J. Lemaire, H. Desvaux, P. Davidson, and P. Batail, Nature (London) **413**, 504 (2001).
[22] N. Miyamoto and T. Nakato, J. Phys. Chem. B **108**, 1652 (2004).
[23] D. van der Beek and H. N. M. Lekkerkerker, Langmuir **20**, 8582 (2004).
[24] N. Wang, S. Liu, J. Zhang, Z. Wu, J. Chen, and D. Sun, Soft Matter **1**, 428 (2005).
[25] A. V. Petukhov, D. van der Beek, R. P. A. Dullens, I. P. Dolbnya, G. J. Vroege, and H. N. W. Lekkerkerker, Phys. Rev. Lett. **95**, 077801 (2005).
[26] D. Sun, H.-J. Sue, Z. Cheng, Y. Martínez-Ratón, and E. Velasco, Phys. Rev. E **80**, 041704 (2009).
[27] G. J. Vroege, D. M. E. Thies-Weesie, A. V. Petukhov, B. J. Lemaire, and P. Davidson, Adv. Mater. **18**, 2565 (2006).
[28] In the platelike particle system, both of the terms "smectic" and "lamellar" are often used for indicating the same LC phase, which has one-dimensional periodic order. Hereafter to avoid the confusion the term "lamellar" is consistently used for representing the smectic or lamellar LC phase where particles are arranged to have a long-range periodic order along their normal axis **a** [see Fig. 1(a1)] but to show only liquidlike short-range order among their neighboring particles in the direction perpendicular to the normal axis.
[29] H. Ringsdorf, R. Wüstefeld, E. Zerta, M. Ebert, and J. H. Wendorff, Angew. Chem. Int. Ed. Engl. **28**, 914 (1989).
[30] H. Ringsdorf and R. Wüstefeld, in *Molecular Chemistry for Electronics*, edited by P. Day, D. C. Bradley, and D. Bloor (The Royal Society, London, 1990), p. 23.
[31] H. Ringsdorf and R. Wüstefeld, Phil. Trans. R. Soc. A **330**, 95 (1990).
[32] R. Hosemann and S. N. Bagchi, *Direct Analysis of Diffraction by Matter* (North-Holland, Amsterdam, 1962).
[33] T. Takebe, T. Hashimoto, B. Ernst, P. Navard, and R. S. Stein, J. Chem. Phys. **92**, 1366 (1990).
[34] L. J. Michot, I. Bihannic, S. Maddi, C. Baravian, P. Levitz, and P. Davidson, Langmuir **24**, 3127 (2008).
[35] L. J. Michot, C. Baravian, I. Bihannic, S. Maddi, C. Moyne, J. F. L. Duval, P. Levitz, and P. Davidson, Langmuir **25**, 127 (2009).
[36] E. Paineau *et al.*, J. Phys. Chem. B **113**, 15858 (2009).
[37] E. Paineau, I. Bihannic, C. Baravian, A.-M. Philippe, P. Davidson, P. Levitz, S. S. Funari, C. Rochas, and L. J. Michot, Langmuir **27**, 5562 (2011).
[38] E. Paineau, L. J. Michot, I. Bihannic, and C. Baravian, Langmuir **27**, 7806 (2011).
[39] N. I. Ringdal, D. M. Fonseca, E. L. Hansen, H. Hemmen, and J. O. Fossum, Phys. Rev. E **81**, 041702 (2010).
[40] N. Miyamato, H. Iijima, H. Ohkubo, and Y. Yamauchi, Chem. Commun. **46**, 4166 (2010).
[41] As for the (hexagonal) columnar phase, we could not find any trace of it in this study, despite the fact that it is not only predicted to have a stability range between the nematic and solid phases [11] but also confirmed by a number of experimental studies [19,20,23,25]. This discrepancy is beyond the scope of this study, though its clarification deserves future works for deeper insight into the formation mechanism of the LC phases of platelike particles.
[42] $\phi_p^* = 8.9\times10^{-5}$–$1.7\times10^{-3}$ for the rigid plates with $L = 12.2$–0.65 μm or $\phi_p^* = 0.014$ for flexible plates with $L = l_p \sim (2\pi/0.08)$ nm ~ 80 nm for $L = 0.98$ μm at $\phi_p^* = 0.01$ [see profile (iii) in Fig. 4(c)].
[43] M. Kestigian, F. D. Leipziger, J. R. Carter, and F. G. Garabedian, J. Am. Ceram. Soc. **49**, 517 (1966).
[44] T. Nakato and N. Miyamoto, J. Mater. Chem. **12**, 1245 (2002).
[45] N. Miyamoto, H. Yamamoto, R. Kaito, and K. Kuroda, Chem. Commun. 2378 (2002).
[46] S. Koizumi, H. Iwase, J. Suzuki, T. Oku, R. Motokawa, H. Sasao, H. Tanaka, D. Yamaguchi, H. M. Shimizu, and T. Hashimoto, J. Appl. Crystallogr. **40**, s474 (2007).

[47] K. Inoue, T. Oka, T. Suzuki, N. Yagi, K. Takeshita, S. Goto, and T. Ishikawa, J. Nucl. Instrum. Methods A **467-468**, 674 (2001).
[48] N. Ohta, T. Oka, K. Inoue, N. Yagi, S. Kato, and I. Hatta, J. Appl. Crystallogr. **38**, 274 (2005).
[49] Since the thickness of the sample cell is 1 mm for the SAXS measurements for (v) shown in Fig. 4(b), there is a considerable space for a large number of small nematic grains of nanosheets aligned with their directions $\mathbf{n}_G$'s randomly along the propagation direction of incident x-ray beam and give rise to a circular scattering pattern. For instance, if the nematic grain is a cube of 5.5 μm each side, there are $1000/5.5 \sim 180$ grains along the beam direction, each of which is consisting of $(\frac{5.5}{0.65})^2 \frac{5.5}{(2\pi/0.1)\times 10^{-3}} \sim 6 \times 10^3$ nanosheets, so that $\mathbf{n}$ can have a random orientation mediated by the disclinations.
[50] J. Perrin, *Les atomes* (Félix Alcan, Paris, 1913) [English translation]; J. Perrin, *Atoms* (Constable, London, 1916).
[51] R. van Roij, J. Phys.: Condens. Matter **15**, S3569 (2003).
[52] M. Doi and A. Onuki, J. Phys. II **2**, 1631 (1992).
[53] A. Onuki, *Phase Transition Dynamics* (Cambridge University Press, Cambridge, 2002).
[54] T. Hashimoto, J. Polym. Sci., Part B: Polym. Phys. **42**, 3027 (2004).
[55] T. Hashimoto, Bull. Chem. Soc. Jpn. **78**, 1 (2005).
[56] A. Onuki, J. Chem. Phys. **85**, 1122 (1986).
[57] T. Hashimoto, Phase Transitions **12**, 47 (1988).
[58] H. Tanaka, Macromolecules **25**, 6377 (1992).
[59] H. Tanaka, Phys. Rev. Lett. **71**, 3158 (1993).
[60] H. Tanaka, J. Chem. Phys. **100**, 5253 (1994).
[61] H. Tanaka, Phys. Rev. Lett. **76**, 787 (1996).
[62] N. Toyoda, M. Takenaka, S. Saito, and T. Hashimoto, Polymer **42**, 9193 (2001).
[63] M. Takenaka, H. Takeno, H. Hasegawa, S. Saito, T. Hashimoto, and M. Nagao, Phys. Rev. E **65**, 021806-1 (2002).
[64] S. Chandrasekhar, *Hydrodynamic and Hydromagnetic Stability* (Dover, Oxford, 1961), Chap. IX.
[65] D. van der Beek, T. Schilling, and H. N. W. Lekkerkerker, J. Chem. Phys. **121**, 5423 (2004), and the earlier representative studies of the effect of sedimentation on the colloidal systems are cited therein.
[66] E. van den Pol, D. M. E. Thies-Weesie, A. V. Petukhov, G. J. Vroege, and K. Kvashnina, J. Chem. Phys. **129**, 164715 (2008).
[67] E. van den Pol, A. V. Petukhov, D. M. E. Thies-Weesie, D. V. Byelov, and G. J. Vroege, Phys. Rev. Lett. **103**, 258301 (2009).
[68] G. Y. Onoda, Phys. Rev. Lett. **55**, 226 (1985).
[69] H. Yoshida, N. Ise, and T. Hashimoto, J. Chem. Phys. **103**, 10146 (1995).
[70] H. Maeda and Y. Maeda, Phys. Rev. Lett. **90**, 018303 (2003).
[71] A. Stradner, H. Sedgwick, F. Cardinaux, W. C. K. Poon, S. U. Egelhaaf, and P. Schurtenberger, Nature (London) **432**, 492 (2004).
[72] Here $\phi_{\mathrm{p\,nematic}}$ is the bulk concentration of the sheets in the nematic phase and obtained under the following two assumptions: (1) The volume ratio of the nematic to isotropic phase is estimated as 9:1 from Fig. 4(a) (α); (2) Approximately all the nanosheets reside in the nematic phase based on the fact that the SAXS pattern of Fig. 4(b) (i) exhibits nearly no signal from nanosheets.
[73] P. A. Forsyth Jr., S. Marčelja, D. J. Mitchell, and B. W. Ninham, J. Chem. Soc., Faraday Trans. 2 **73**, 84 (1977).
[74] P. A. Forsyth Jr., S. Marčelja, D. J. Mitchell, and B. W. Ninham, Adv. Colloid Interface Sci. **9**, 37 (1978).
[75] B. V. Derjaguin and L. D. Landau, Acta Physicochim. URSS **14**, 633 (1941).
[76] E. J. W. Verwey and J. Th. G. Overveek, *Theory of the Stability of Lyophobic Colloids* (Elsevier, Amsterdam, 1948).
[77] I. Sogami, Phys. Lett. A **96**, 199 (1983).
[78] M. V. Smalley, Langmuir **10**, 2884 (1994).
[79] P. Linse and V. Lobaskin, Phys. Rev. Lett. **83**, 4208 (1999).
[80] H. Boroudjerdi, Y.-W. Kim, A. Naji, R. R. Netz, X. Schlagberger, and A. Serr, Phys. Rep. **416**, 129 (2005).
[81] J. N. Israelacvili, Proc. R. Soc. Lond. A. **331**, 39 (1972).
[82] A. Caillé, C. R. Acad. Sci. Paris B **274**, 891 (1972).
[83] J. Als-Nielsen, J. D. Litster, R. J. Birgeneau, M. Kaplan, C. R. Safinya, A. Lindegaard-Andersen, and S. Mathiesen, Phys. Rev. B **22**, 312 (1980).
[84] L. Gunther, Y. Imry, and J. Lajzerowicz, Phys. Rev. A **22**, 1733 (1980).
[85] C. R. Safinya, D. Roux, G. S. Smith, S. K. Sinha, P. Dimon, N. A. Clark, and A. M. Bellocq, Phys. Rev. Lett. **57**, 2718 (1986).
[86] D. Roux and C. R. Safinya, J. Phys. (Paris) **49**, 307 (1988).
[87] D. C. Wack and W. W. Webb, Phys. Rev. A **40**, 1627 (1989).
[88] F. Nallet, R. Laversanne, and D. Roux, J. Phys. II Fr. **3**, 487 (1993).
[89] R. Zhang, R. M. Suter, and J. F. Nagle, Phys. Rev. E **50**, 5047 (1994).
[90] W. H. de Jeu, B. I. Ostrovskii, and A. N. Shalaginov, Rev. Mod. Phys. **75**, 181 (2003).
[91] Other outstanding studies on this issue have been carried out by using x-ray reflectivity. The list of those studies is cited in Ref. [90].